

1
2
3
4
5
6
7
8
9
10
11
12
13 **The Development of the North Pacific Jet Phase Diagram as an Objective Tool to Monitor**
14 **the State of the Upper-Tropospheric Flow Pattern**

15
16 *By*

17
18 ANDREW C. WINTERS^{1*}, DANIEL KEYSER¹, and LANCE F. BOSART¹

19
20 ¹Department of Atmospheric and Environmental Sciences
21 University at Albany, State University of New York
22 Albany, NY 12222
23
24
25
26
27
28

29 Submitted for publication in _____
30 XX XXX 2018
31
32
33
34
35
36
37
38
39
40
41
42
43
44

* *Corresponding author address:* Andrew C. Winters, Dept. of Atmospheric and Environmental Sciences,
University at Albany, SUNY, 1400 Washington Ave., Albany, NY 12222. E-mail: acwinters@albany.edu

ABSTRACT

Previous studies employing empirical orthogonal function (EOF) analyses of upper-tropospheric zonal wind anomalies have identified the leading modes of North Pacific jet (NPJ) variability that prevail on synoptic time scales. The first leading mode corresponds to a zonal extension or retraction of the exit region of the climatological NPJ, while the second leading mode corresponds to a poleward or equatorward shift of the exit region of the climatological NPJ. These NPJ regimes can strongly influence the character of the large-scale flow pattern over North America. Consequently, knowledge of the prevailing NPJ regime and the forecast skill associated with each NPJ regime has the potential to increase confidence in operational medium-range (6–10-day) forecasts over North America.

This study documents the development of a NPJ Phase Diagram, which is constructed from the two leading EOFs of 250-hPa zonal wind anomalies during September–May 1979–2014. The projection of 250-hPa zonal wind anomalies at one or multiple times onto the NPJ Phase Diagram provides an objective characterization of the state or evolution of the upper-tropospheric flow pattern over the North Pacific. A 30-year analysis of GEFS reforecasts with respect to the NPJ Phase Diagram demonstrates that forecasts initialized and verified during jet retraction and equatorward shift regimes are associated with larger average errors than jet extension and poleward shift regimes. An examination of the best and worst forecasts further suggests that periods characterized by rapid NPJ regime transition or the development and maintenance of North Pacific blocking events exhibit reduced forecast skill.

1. Introduction

Anchored downstream of the Asian continent at middle latitudes, the North Pacific jet (NPJ) stream is a narrow, meandering current of strong upper-tropospheric wind speeds bounded by appreciable horizontal and vertical shear. The position and intensity of the NPJ is modulated by a number of external factors, including tropical convection (e.g., Hoskins and Karoly 1981; Madden and Julian 1994; Harr and Dea 2009; Archambault et al. 2013, 2015; Torn and Hakim 2015; Grams and Archambault 2016; Bosart et al. 2017), interactions between the NPJ and baroclinic eddies along the midlatitude storm track (e.g., Orlanski and Sheldon 1995; Chang et al. 2002; Hakim 2003; Torn and Hakim 2015; Bosart et al. 2017), and the East Asian Winter Monsoon (e.g., Jhun and Lee 2004; Lee et al. 2010; Wang and Chen 2014; Handlos and Martin 2016). In combination, these factors contribute to NPJ configurations that vary substantially on both weather and climate time scales.

In an attempt to characterize the variability of the NPJ, prior work has identified the leading modes of NPJ variability that prevail on weather and climate time scales during the winter (Dec–Feb). Schubert and Park (1991) provided one of the first investigations of subseasonal NPJ variability, and calculated the two leading traditional empirical orthogonal functions¹ (EOFs) of 20–70-day filtered zonal wind at 200 hPa over the Pacific basin. Their first EOF describes variability in the intensity of the NPJ over the western North Pacific, while their second EOF describes a zonal extension or retraction of the exit region of the climatological NPJ. In contrast, Eichelberger and Hartmann (2007) employed daily zonal wind data during January in their traditional EOF analysis and found that the first EOF of the vertically averaged zonal-mean zonal wind over the North Pacific encompasses variability in the intensity,

¹ A traditional EOF analysis is a statistical technique to extract patterns that explain the greatest fraction of the variance within a multidimensional dataset (Wilks 2011).

longitudinal extent, and latitudinal position of the NPJ. Consequently, the Eichelberger and Hartmann (2007) analysis suggests that NPJ variability is considerably more complex when analyzed on synoptic rather than subseasonal time scales.

Recent studies by Athanasiadis et al. (2010) and Jaffe et al. (2011) provided additional physical clarity on the two leading modes of NPJ variability that prevail on synoptic time scales during the cold season (Nov–Mar). These studies applied traditional EOF analysis to unfiltered upper-tropospheric zonal wind data over the North Pacific and determined that the first mode of NPJ variability corresponds to longitudinal variability in the vicinity of the exit region of the climatological NPJ. Specifically, a positive EOF 1 pattern (+EOF 1) describes a zonal extension of the exit region of the climatological NPJ, while a negative EOF 1 pattern (–EOF 1) describes a zonal retraction of the exit region of the climatological NPJ. The second mode of NPJ variability corresponds to latitudinal variability in the vicinity of the exit region of the climatological NPJ. In the context of this mode, a positive EOF 2 pattern (+EOF 2) describes a poleward shift of the exit region of the climatological NPJ, while a negative EOF 2 pattern (–EOF 2) describes an equatorward shift.

Knowledge of the four NPJ configurations identified by Athanasiadis et al. (2010) and Jaffe et al. (2011), hereafter referred to as NPJ regimes, subsequently permits an examination of the relationship between each NPJ regime and the downstream large-scale flow pattern over North America. To this end, Griffin and Martin (2017) employed time-extended EOF analyses (e.g., Weare and Nasstrom 1982; Wilks 2011) of 250-hPa zonal wind data from the NCEP/NCAR reanalysis dataset (Kalnay et al. 1996) to construct composite analyses of the large-scale flow evolution over the North Pacific and North America during the 10-day period preceding and following the development of each NPJ regime. The Griffin and Martin (2017)

analysis yields a clear relationship between each NPJ regime and the large-scale flow pattern over North America, and implies that knowledge of the prevailing NPJ regime may offer considerable value to operational medium-range (6–10-day) forecasts of temperature and precipitation over North America. However, this value is limited operationally without complementary knowledge of the relative forecast skill associated with the development or persistence of each NPJ regime.

The concept of regime-dependent forecast skill has been explored with respect to large-scale upper-tropospheric flow regimes over the North Atlantic basin (e.g., Ferranti et al. 2015) and with respect to large-scale atmospheric teleconnection patterns (e.g., Palmer 1988; Lin and Derome 1996; Sheng 2002; Ferranti et al. 2015). However, to the authors' knowledge, no study has comprehensively examined regime-dependent forecast skill over the North Pacific with respect to the prevailing NPJ regime. Consequently, a primary goal of the present study is to identify whether certain NPJ regimes exhibit enhanced or reduced forecast skill. In an effort to address this goal, the results from prior studies on NPJ variability (e.g., Athanasiadis et al. 2010; Jaffe et al. 2011; Griffin et al. 2017) are extended to the cool season (Sep–May) and a two-dimensional phase diagram, hereafter referred to as the NPJ Phase Diagram, is developed employing the two leading modes of NPJ variability during that time period. The NPJ Phase Diagram subsequently aids in visualizing the state and evolution of the upper-tropospheric flow pattern over the North Pacific, and serves as an objective tool from which new insights can be derived regarding the climatology and forecast skill of each NPJ regime.

The remainder of this manuscript is structured as follows. Section 2 discusses the development of the NPJ Phase Diagram. Section 3 discusses the climatology of each NPJ regime and reviews the large-scale flow patterns associated with each NPJ regime. Section 4 examines

the forecast skill of each NPJ regime with respect to the NPJ Phase Diagram. Section 5 illuminates the characteristics of the best and worst forecast periods with respect to the NPJ Phase Diagram, and section 6 offers a discussion of the results and some conclusions.

2. Development of the NPJ Phase Diagram

The NPJ Phase Diagram is developed by employing anomalies of the zonal component of the 250-hPa vector wind from the 0.5°-resolution National Centers for Environmental Prediction Climate Forecast System Reanalysis (CFSR; Saha et al. 2010, 2014) at 6-h intervals during September–May 1979–2014. Anomalies are calculated as the deviation of the instantaneous 250-hPa zonal wind from a 21-day running mean centered on each analysis time in order to remove the 36-year mean as well as the annual and diurnal cycles. The CFSR is chosen for this study because of its role in providing the initial conditions for the Global Ensemble Forecast System (GEFS) Reforecast Version 2 dataset prior to 2011 (Hamill et al. 2013). The GEFS Reforecast dataset is utilized in sections 4 and 5 to examine the forecast skill of each NPJ regime with respect to the NPJ Phase Diagram. A traditional EOF analysis (Wilks 2011) is subsequently performed on the 250-hPa zonal wind anomaly data within a horizontal domain bounded in latitude from 10°N to 80°N and in longitude from 100°E to 120°W in order to identify the two leading modes of NPJ variability. This horizontal domain is chosen to capture the entire North Pacific basin and to match the domain employed by Griffin and Martin (2017).

In comparison to traditional EOF analysis, Griffin and Martin (2017) demonstrate that time-extended EOF analysis (e.g., Weare and Nasstrom 1982; Wilks 2011) of 250-hPa zonal wind anomalies over the North Pacific is beneficial for ensuring that the evolution of the NPJ is characterized by a higher degree of temporal coherence. However, this higher degree of temporal coherence is achieved by filtering out the high-frequency variability of the NPJ that occurs on

daily time scales (Griffin and Martin 2017; their Fig. 1). When considering the NPJ and its influence on the downstream upper-tropospheric flow pattern over North America, short-term fluctuations in the position, intensity, and evolution of the NPJ, such as those associated with recurving tropical cyclones or intensifying extratropical cyclones, can have substantial impacts on the character of the downstream upper-tropospheric flow pattern over North America (e.g., Archambault et al. 2015; Torn and Hakim 2015; Grams and Archambault 2016; Bosart et al. 2017). Additionally, the application of time-extended EOF analysis is computationally more expensive than traditional EOF analysis, especially when employing a dataset with 0.5° resolution such as the CFSR. For these two reasons, traditional EOF analysis is chosen for this study. The subsequent analysis demonstrates that the application of traditional EOF analysis to 250-hPa zonal wind anomalies during the cool season from the CFSR produces the same two leading modes of NPJ variability as found in previous studies (Athanasiadis et al. 2010; Jaffe et al. 2011; Griffin and Martin 2017).

The regression of 250-hPa zonal wind anomalies from the CFSR onto the two leading spatial patterns obtained from the traditional EOF analysis, EOF 1 and EOF 2, are illustrated in Fig. 1. The sign of a particular EOF pattern is arbitrary, but is chosen in Fig. 1 to ensure consistency with previous studies on NPJ variability. EOF 1 explains 12.2% of the variance of 250-hPa zonal wind over the North Pacific and corresponds to longitudinal variability of the 250-hPa zonal wind in the vicinity of the exit region of the climatological NPJ. A positive EOF 1 pattern (+EOF 1) is associated with a zonal extension of the exit region of the climatological NPJ (i.e., a jet extension), while a negative EOF 1 pattern (–EOF 1) is associated with a retraction of the exit region of the climatological NPJ (i.e., a jet retraction). EOF 2 explains 8.8% of the variance of 250-hPa zonal wind over the North Pacific and corresponds to latitudinal variability

of the 250-hPa zonal wind in the vicinity of the exit region of the climatological NPJ. A positive EOF 2 pattern (+EOF 2) is associated with a poleward shift of the exit region of the climatological NPJ (i.e., a poleward shift), while a negative EOF 2 pattern (–EOF 2) is associated with an equatorward shift of the exit region of the climatological NPJ (i.e., an equatorward shift). The combined variance explained by EOF 1 and EOF 2 is comparable to that found in previous studies (Athanasiadis et al. 2010; Jaffe et al. 2011; Griffin and Martin 2017) and the two leading EOFs are statistically well separated using the methodology outlined in North et al. (1982). To ensure that the EOF patterns shown in Fig. 1 are representative of the entire cool season, separate traditional EOF analyses were performed on three-month subsets of the 250-hPa zonal wind anomaly data. These independent EOF analyses (not shown) confirm that EOF 1 and EOF 2 represent the two leading modes of NPJ variability with fidelity throughout the cool season.

The 250-hPa zonal wind anomalies at any particular analysis time can be regressed onto EOF 1 and EOF 2 to calculate the instantaneous principal components (PCs), PC 1 and PC 2, corresponding to that analysis time. The magnitude and sign of PC 1 and PC 2 are standardized and provide an indication of how strongly the instantaneous 250-hPa zonal wind anomalies project onto EOF 1 and EOF 2, respectively. Time series constructed from the instantaneous PCs subsequently assist in characterizing the temporal evolution of the NPJ with respect to EOF 1 and EOF 2. As noted by Griffin and Martin (2017), the use of instantaneous PCs produces a noisy time series due to the high-frequency variability that characterizes the NPJ on daily time scales (their Fig. 1). Consequently, in an attempt to describe the evolution of the NPJ with greater temporal coherence than the instantaneous PCs while preserving the high-frequency variability of the NPJ on daily time scales, the instantaneous PCs are smoothed through the

calculation of a weighted average of the instantaneous PCs within ± 24 h of each analysis time, t_0 . The weight, w , prescribed to the instantaneous PCs at each analysis time, t , within ± 24 h of t_0 is defined as: $w = 5 - |t - t_0|/6$, for $|t - t_0| \leq 24$ h.

The weighted PCs at a particular analysis time can then be plotted on a two-dimensional Cartesian grid (i.e., the NPJ Phase Diagram) in an effort to visualize the state of the NPJ. The position along the abscissa within the NPJ Phase Diagram corresponds to the value of weighted PC 1 and indicates how strongly the 250-hPa zonal wind anomalies project onto EOF 1. Positive and negative values of weighted PC 1 represent a jet extension and jet retraction, respectively. The position along the ordinate within the NPJ Phase Diagram corresponds to the value of weighted PC 2 and indicates how strongly the 250-hPa zonal wind anomalies project onto EOF 2. Positive and negative values of weighted PC 2 represent a poleward shift and equatorward shift, respectively. Salient examples of NPJ configurations that project strongly onto a jet extension and a jet retraction regime are provided in Figs. 2a and 2b, respectively, while NPJ configurations that project strongly onto a poleward shift and an equatorward shift regime are provided in Figs. 3a and 3b, respectively.

As for the sample cases shown in Figs. 2 and 3, the weighted PCs at all analysis times during September–May 1979–2014 are plotted on the NPJ Phase Diagram in order to classify each analysis time into one of the four NPJ regimes, or to identify analysis times during which the NPJ lies within the unit circle (Fig. 4). For this classification scheme, the analysis times are classified based on, first, whether the position of the NPJ within the NPJ Phase Diagram is greater than a distance of 1 PC unit from the origin and, second, whether the absolute value of PC 1 or PC 2 is greater. Analysis times that fall into the “origin” category are interpreted as times during which the NPJ exhibits a neutral signal with respect to the NPJ Phase Diagram.

Plotting the weighted PCs onto the NPJ Phase Diagram over a specified time interval captures the evolution of the NPJ and yields a trajectory within the NPJ Phase Diagram.

3. Characteristics of the NPJ Phase Diagram

The classification of analysis times discussed in section 2 illuminates several salient characteristics of each NPJ regime. The typical residence time of the NPJ within each NPJ regime is provided in Table 1. Overall, the mean and median residence time within an NPJ regime do not vary considerably between the NPJ regimes. Specifically, the mean residence time within an NPJ regime ranges between 3.58 and 3.85 days, while the median residence time ranges between 2.50 and 2.75 days. The residence time is slightly longer for periods when the NPJ resides within the unit circle, with a mean and median residence time of 4.65 and 3.25 days, respectively. The inequality between the mean and median residence times for each NPJ regime highlights the degree to which the distribution of residence times is skewed towards transient rather than persistent NPJ regimes. In support of this observation, an examination of the minimum and maximum residence time within each NPJ regime indicates that while an NPJ regime can be transient, it can also persist for multiple weeks.

As demonstrated from previous studies on NPJ variability, each NPJ regime exhibits a strong influence on the character of the downstream large-scale flow pattern over North America (e.g., Athanasiadis et al. 2010; Jaffe et al. 2011; Griffin and Martin 2017). To ensure consistency with previous studies, composite analyses are constructed employing the CFSR for periods during which the NPJ resided within the same NPJ regime for at least three consecutive days. A three-day threshold is chosen as a compromise between the magnitude of the mean and median residence time for each NPJ regime (Table 1). Figures 5 and 6 illustrate the characteristic large-scale flow pattern four days following the onset of each NPJ regime. This particular time is

subjectively chosen for brevity and to highlight both the characteristic structure of the NPJ, as well as the downstream flow pattern over North America associated with each NPJ regime. Two-sided Student's t-tests were performed on the geopotential height and temperature anomaly fields shown in Figs. 5 and 6 to identify anomalies that are statistically significant with respect to climatology at the 99% confidence level. The reader is referred to Griffin and Martin (2017) for further detail on the evolution of the large-scale flow pattern associated with each NPJ regime.

A jet extension (N=159) is characterized by the meridional juxtaposition of an anomalous upper-tropospheric trough over the central North Pacific and an anomalous ridge over the subtropical North Pacific that combine to produce a strong, zonally-oriented NPJ (Fig. 5a). Beneath the left-exit region of the extended NPJ, an anomalous surface cyclone drives anomalous southerly geostrophic flow along the west coast of North America (Fig. 6a). This southerly geostrophic flow is associated with the development of lower-tropospheric warm anomalies over western North America and, subsequently, the amplification of an anomalous upper-tropospheric ridge in the same location (Fig. 5a). Lower-tropospheric cold anomalies are found upstream of the surface cyclone in conjunction with anomalous northerly geostrophic flow over the central North Pacific, and across eastern North America beneath an anomalous upper-tropospheric trough (Fig. 6a).

A jet retraction (N=162) features an anomalous upper-tropospheric ridge over the central North Pacific, and anomalous troughs over northwestern North America and the subtropical North Pacific (Fig. 5b). In combination, these geopotential height anomalies result in a retracted NPJ over the western North Pacific and a split NPJ to the east of the dateline. Directly beneath the central North Pacific ridge, the circulation associated with an anomalous surface anticyclone contributes to the development of lower-tropospheric cold anomalies over Alaska and the west

coast of North America, and warm anomalies over the central North Pacific (Fig. 6b). Lower-tropospheric warm anomalies are also found in the south-central U.S. upstream of an anomalous upper-tropospheric ridge positioned over the southeastern U.S.

A poleward shift (N=189) exhibits an anomalous upper-tropospheric trough over the high-latitude North Pacific and an anomalous ridge over the subtropical North Pacific that act in combination to position the exit region of the NPJ poleward of 40°N (Fig. 5c). An anomalous surface cyclone is located beneath the left-exit region of the poleward-shifted NPJ, which results in anomalous southerly geostrophic flow over northern North America and the development of lower-tropospheric warm anomalies in that location (Fig. 6c). These lower-tropospheric warm anomalies are also associated with an anomalous upper-tropospheric ridge positioned over eastern Canada (Fig. 5c). Lower-tropospheric cold anomalies are only observed over the Bering Strait and Gulf of Alaska during a poleward shift in conjunction with anomalous northerly geostrophic flow upstream of the surface cyclone (Fig. 6c).

Lastly, an equatorward shift (N=149) is associated with an anomalous upper-tropospheric ridge over the high-latitude North Pacific and an anomalous trough over the subtropical North Pacific, reminiscent of a Rex block (Fig. 5d; Rex 1950). This configuration of geopotential height anomalies results in an equatorward deflection of the exit region of the NPJ near Hawaii, and a weaker NPJ over the western North Pacific compared to the other NPJ regimes. An anomalous upper-tropospheric trough is also positioned over eastern Canada downstream of the high-latitude ridge over the North Pacific (Fig. 5d). In the lower-troposphere, an equatorward shift is associated with an anomalous surface anticyclone centered near the Aleutian Islands. This surface anticyclone facilitates anomalous northerly geostrophic flow over northern North America and the development of lower-tropospheric cold anomalies in that location (Fig. 6d).

Conversely, anomalous southerly geostrophic flow upstream of the surface anticyclone contributes to the development of lower-tropospheric warm anomalies over the Bering Strait and the Gulf of Alaska.

Additional insight is found by considering the interannual and intraannual variability of each NPJ regime. While the NPJ resides within one of the four NPJ regimes (i.e., outside a radius of 1 PC unit from the origin) 59% of the time during an average cool season (not shown), there is considerable interannual variability in the frequency of each NPJ regime (Fig. 7a). As an example, the 1997–1998 cool season was characterized by the second-lowest annual frequency of poleward shifts (4.7%), while the subsequent 1998–1999 cool season featured highest annual frequency of poleward shifts (34.9%). Comparable abrupt changes in the annual frequency of an individual NPJ regime are readily observed when considering the time series for other NPJ regimes, as well. Furthermore, linear regressions performed on each of the time series shown in Fig. 7a do not identify any statistically significant trends in the frequency of each NPJ regime during 1979–2014 (not shown).

Substantial variability characterizes the frequency of each NPJ regime throughout the duration of an individual cool season, as well (Fig. 7b). Specifically, the NPJ resides within an NPJ regime most frequently during November–March and less frequently during the months of September, October, April, and May. Both jet extensions and jet retractions peak in frequency during the month of March, while poleward shifts and equatorward shifts peak during February and January, respectively. The frequencies of each NPJ regime during an individual month are generally comparable, except during March, when jet extensions and jet retractions are noticeably more frequent than poleward shifts and equatorward shifts, and during September,

when poleward shifts and equatorward shifts are nearly two times more frequent than jet extensions and jet retractions.

As may be anticipated, the interannual and intraannual frequency of each NPJ regime are strongly modulated by large-scale atmospheric teleconnection patterns. For example, the Pacific/North American (PNA) pattern is known to exhibit a strong relationship with the intensity of the NPJ (e.g., Wallace and Gutzler 1981; Barnston and Livezey 1987; Franzke and Feldstein 2005; Strong and Davis 2008; Athanasiadis et al. 2010; Franzke et al. 2011; Griffin and Martin 2017). Specifically, a positive PNA pattern is canonically characterized by an anomalous upper-tropospheric trough over the central North Pacific and an anomalous ridge over the subtropical North Pacific. Consequently, a positive PNA pattern is particularly conducive to the development of an extended NPJ. Conversely, a negative PNA pattern exhibits an anomalous upper-tropospheric ridge over the central North Pacific that favors a retracted NPJ.

To clearly illustrate the relationship between the PNA and each NPJ regime, all analysis times that were characterized by a NPJ regime (i.e., outside a radius of 1 PC unit from the origin) were classified based on the sign and magnitude of the daily PNA index (CPC 2017a). Analysis times that featured a PNA index > 0.5 were classified as occurring during a positive PNA, those that featured a PNA index < -0.5 were classified as occurring during a negative PNA, and those remaining were classified as occurring during a neutral PNA. Figure 8a demonstrates that the frequency of each NPJ regime is indeed well associated with the phase of the PNA, with jet extensions and poleward shifts occurring most frequently during a positive PNA, and jet retractions and equatorward shifts occurring most frequently during a negative PNA.

The frequency of each NPJ regime also exhibits an association with the phase of the Arctic Oscillation (AO; Thompson and Wallace 1998; Higgins et al. 2000; Ambaum et al. 2001).

The positive phase of the AO is canonically characterized by above-normal 1000-hPa geopotential heights over the central North Pacific and below-normal 1000-hPa geopotential heights over the Arctic. As for the PNA index, daily AO indices (CPC 2017b) are employed to classify analysis times that were characterized by a NPJ regime. Those analysis times exhibiting an AO index > 0.5 were classified as occurring during a positive AO, those exhibiting an AO index < -0.5 were classified as occurring during a negative AO, and those remaining were classified as occurring during a neutral AO. Figure 8b indicates that jet retractions are most frequent during a positive AO and jet extensions are most frequent during a negative AO. This relationship agrees with the NPJ regime composites shown in Fig. 6, given that jet retractions are associated with an anomalous surface anticyclone over the central North Pacific (Fig. 6b), and jet extensions feature an anomalous surface cyclone in that location (Fig. 6a).

The El Niño–Southern Oscillation (ENSO) can also modulate the structure of the NPJ. For example, prior work suggests that anomalous convection and above-normal sea-surface temperatures over the central and eastern equatorial Pacific during an El Niño favor an extended and equatorward-shifted NPJ. Conversely, anomalous convection and above-normal sea-surface temperatures over the western equatorial Pacific during a La Niña favor a retracted NPJ (e.g., Horel and Wallace 1981; Rasmusson and Wallace 1983; Rasmusson and Mo 1993; Yang et al. 2002; Xie et al. 2015; Cook et al. 2017). In an effort to frame this relationship with respect to the NPJ Phase Diagram, analysis times that were characterized by a NPJ regime were classified based on the sign and magnitude of the monthly Nino3.4 index (ESRL 2017). Any analysis times that coincided with a Nino3.4 index > 1.0 were classified as occurring during an El Niño, analysis times that coincided with a Nino3.4 index < -1.0 were classified as occurring during a La Niña, and all other analysis times were classified as occurring during a neutral ENSO state.

Figure 8c demonstrates that El Niño is indeed most frequently characterized by jet extensions and equatorward shifts. Conversely, La Niña is most frequently characterized by jet retractions and poleward shifts. The results from Fig. 8c translate to individual cool seasons characterized by El Niño and La Niña events, as well. For example, Fig. 7a indicates that the 1982–1983 El Niño cool season (Sep–May Nino3.4 = 1.82) was most frequently characterized by jet extensions and equatorward shifts, while the 1999–2000 La Niña cool season (Sep–May Nino3.4 = −1.22) was most frequently characterized by jet retractions and poleward shifts.

4. GEFS forecast skill with respect to the NPJ Phase Diagram

Provided with a relationship between each NPJ regime and the downstream large-scale flow pattern over North America, complementary knowledge of the forecast skill associated with each NPJ regime offers the potential to increase confidence in operational medium-range forecasts over North America. To evaluate the forecast skill associated with each NPJ regime, an ensemble of 9-day forecast trajectories within the NPJ Phase Diagram are calculated daily during September–May 1985–2014 using 250-hPa zonal wind data from the 1.0°-resolution GEFS Reforecast Version 2 dataset (Hamill et al. 2013). The GEFS Reforecast dataset features 10 ensemble member forecasts and 1 control member forecast initialized daily at 0000 UTC, each with forecast lead times as long as 384 h.

Forecast errors within the NPJ Phase Diagram are calculated as the distance error in PC units between the ensemble mean NPJ Phase Diagram forecast and the verifying 0-h analysis that corresponds to each forecast lead time. The NPJ Phase Diagram forecasts are then classified (1) based on the position of the NPJ within the NPJ Phase Diagram at the time of forecast initialization or forecast verification following the schematic shown in Fig. 4, and (2) based on season. Two-sided Student’s t-tests are performed on all NPJ Phase Diagram forecast error

statistics to indicate statistical significance in accordance with the criteria outlined in each pertinent figure caption.

The average distance errors associated with ensemble mean NPJ Phase Diagram forecasts initialized during the same season are provided in Fig. 9a. Overall, NPJ Phase Diagram forecasts initialized during the winter (Dec–Feb) exhibit significantly larger distance errors within the NPJ Phase Diagram than forecasts initialized during the fall (Sep–Nov) and spring (Mar–May) at forecast lead times less than 144 h. At lead times greater than 144 h, forecasts initialized during the winter and spring exhibit significantly larger distance errors than forecasts initialized during the fall. Furthermore, forecasts initialized during the fall exhibit distance errors that fall below the cool-season average at all forecast lead times, while forecasts initialized during the winter exhibit errors that lie above the cool-season average at all forecast lead times.

The average distance errors of ensemble mean NPJ Phase Diagram forecasts initialized during the same NPJ regime are shown in Fig. 9b. At lead times less than 120 h, no significant differences in distance error are observed between the NPJ regimes. However, significant differences between the NPJ regimes begin to emerge at lead times greater than 120 h. Specifically, forecasts initialized during a jet retraction exhibit significantly larger distance errors than forecasts initialized during a poleward shift at lead times between 120–168 h, and significantly larger distance errors than forecasts initialized during a jet extension at lead times between 192–216 h. However, despite these significant differences at lead times greater than 120 h, the spread in distance errors between the NPJ regimes is generally less than 0.10 PC units during this time period.

Substantially larger spread between the distance errors associated with each NPJ regime is found while considering NPJ Phase Diagram forecasts verified during the same NPJ regime

(Fig. 9c). In particular, forecasts verified during equatorward shifts and jet retractions exhibit significantly larger distance errors than those verified during poleward shifts and jet extensions at lead times greater than 96 h. Consequently, knowledge of the NPJ regime at the time of forecast verification appears to be a greater indicator of forecast skill with respect to the NPJ Phase Diagram than the NPJ regime at the time of forecast initialization. This result implies that enhanced or reduced confidence can be prescribed to a forecast by considering the forecasted evolution of the NPJ with respect to the NPJ Phase Diagram, rather than by considering the state of the NPJ at the time of forecast initialization.

The poor forecast skill of ensemble mean NPJ Phase Diagram forecasts verified during equatorward shifts is also apparent when considering the frequency with which each NPJ regime is overforecast or underforecast in the GEFS Reforecast dataset. Figure 10 demonstrates that equatorward shifts are substantially underforecast by ensemble mean NPJ Phase Diagram forecasts at all lead times compared to the verifying 0-h analyses. Specifically, equatorward shifts are underforecast by nearly 26% at a 216-h lead time, which is at least double the frequency that the other NPJ regimes are underforecast at the same lead time. While all NPJ regimes are generally underforecast by the ensemble mean NPJ Phase Diagram forecasts at lead times greater than 168 h, both jet extensions and poleward shifts are overforecast at lead times less than 168 h.

5. Best and worst NPJ Phase Diagram forecasts

Additional insight into the forecast skill associated with each NPJ regime is found by considering the characteristics of the best and worst NPJ Phase Diagram medium-range forecasts. Such an investigation has the potential to illuminate factors that may contribute to enhanced or reduced forecast skill (e.g., Lillo and Parsons 2017). The best and worst medium-

range forecasts with respect to the NPJ Phase Diagram are identified as those forecasts that rank in the top or bottom 10%, respectively, in terms of both (1) the average GEFS ensemble *mean* distance error of the 192- and 216-h forecasts and (2) the average GEFS ensemble *member* distance error of the 192- and 216-h forecasts. The first criterion provides a measure of forecast accuracy during the medium-range period, while the second criterion provides a measure of forecast precision during the medium-range period.

Figure 11 illustrates a series of hypothetical NPJ Phase Diagram forecasts that would qualify as a best, an intermediate, and a worst forecast with respect to the two criteria identified in the previous paragraph. A best forecast is one in which the ensemble mean forecast exhibits a small distance error, as well as a small average ensemble member distance error. Consequently, a best forecast can be interpreted as one in which the NPJ Phase Diagram forecast is both accurate and precise. The intermediate forecast depicts a situation in which there is a small ensemble mean distance error, but also a large average ensemble member distance error. Consequently, both criteria are not satisfied, and this situation represents one in which the forecast was accurate but not particularly precise. Finally, a worst forecast is a situation that exhibits large ensemble mean distance error and large average ensemble member distance error, or a forecast that was neither accurate or precise.

As a whole, the frequency distribution of the worst NPJ Phase Diagram forecasts features two separate maxima during the cool season, one during December and another during March, with a relative minimum during January (Fig. 12a). The best NPJ Phase Diagram forecasts tend to occur most frequently during the beginning and end of the cool season, but also peak during December. The best and worst NPJ Phase Diagram forecasts are also classified based on the NPJ regime at the time of forecast initialization in Fig. 12b. This frequency distribution indicates that

the worst forecasts initialized disproportionately more than the best forecasts during jet retractions and equatorward shifts, while the best forecasts initialized disproportionately more than the worst forecasts during jet extensions and poleward shifts. The average value of PC 1 and PC 2 at the time of forecast initialization also indicates a preference for the worst forecasts to initialize most frequently during jet retractions and equatorward shifts, and for the best forecasts to initialize most frequently during jet extensions and poleward shifts (Table 2). However, only the values of PC 1 are statistically different between the best and worst forecasts at the time of forecast initialization.

The evolution of the NPJ during the 10-day period following the initialization of a best or worst NPJ Phase Diagram forecast also differs substantially (Table 2). In particular, the average change in PC 2 ($\Delta PC2$) during the 10-day period following a worst forecast indicates a significant movement of the NPJ towards an equatorward shift within the NPJ Phase Diagram, while the 10-day period following a best forecast exhibits a significant movement of the NPJ towards a poleward shift. Additionally, the worst forecast periods feature significantly longer trajectories within the NPJ Phase Diagram compared to the best forecast periods during the 10-day period following forecast initialization. This particular result suggests that the worst forecasts often occur during periods characterized by rapid NPJ regime change, while the best forecast periods are characterized by more persistent upper-tropospheric flow patterns over the North Pacific. This notion aligns well with previous work, which suggests that periods characterized by upper-tropospheric regime change are associated with reduced forecast skill (e.g., Tibaldi and Molteni 1990; Frederiksen et al. 2004; Pelly and Hoskins 2006; Ferranti et al. 2015; Lillo and Parsons 2017).

An examination of the upper-tropospheric flow patterns associated with the best and worst forecast periods offers insight into the types of large-scale flow patterns that are associated with enhanced or reduced forecast skill. This examination is performed by employing the CFSR to construct composite analyses of 250-hPa wind speed, geopotential height, and geopotential height anomalies at the time a best or worst forecast is initialized, as well as at 192 h following forecast initialization. Two-sided Student's t-tests are subsequently used to evaluate whether the difference between geopotential height anomalies associated with the worst and best forecast composites is statistically significant at each time period.

The composite upper-tropospheric flow patterns at the time a best or worst forecast is initialized within each NPJ regime are provided in Fig. 13. At first glance, an examination of the geopotential height anomalies associated with each composite reveals few qualitative differences between the best and worst forecasts initialized during the same NPJ regime. However, a direct calculation of the difference between geopotential height anomalies associated with the worst and best forecasts illuminates some significant features (Fig. 14). In particular, while both the best and worst forecasts initialized during a jet extension are characterized by a strong, zonally-extended NPJ at the time of forecast initialization (Figs. 13a,b), the worst forecasts exhibit significantly higher geopotential height anomalies over the eastern North Pacific compared to the best forecasts (Fig. 14a). Similarly, both the best and worst forecasts initialized during a jet retraction feature an anomalous ridge over the central North Pacific (Figs. 13c,d). However, the worst forecasts exhibit significantly higher geopotential height anomalies over the Gulf of Alaska, and significantly lower geopotential height anomalies over the subtropical North Pacific and the western Great Lakes compared to the best forecasts (Fig. 14b). The lower geopotential height anomalies over the subtropical North Pacific and western Great Lakes associated with the

worst forecast composite also favor a stronger southern stream of the NPJ to the east of the dateline and less pronounced ridging over eastern North America compared to the best forecasts (Figs. 13c,d).

As for jet extensions and jet retractions, the worst forecasts initialized during a poleward shift also exhibit significantly higher geopotential height anomalies over the Gulf of Alaska compared to the best forecasts (Figs. 13e,f and Fig. 14c). The worst forecasts initialized during a poleward shift are also characterized by a more intense NPJ, a stronger jet stream over North America, and significantly lower geopotential height anomalies over the southwestern U.S. and northwestern Mexico. (Figs. 13e,f and Fig. 14c). While not as prominent as observed in the other composites, the worst forecasts initialized during an equatorward shift also exhibit significantly higher geopotential height anomalies over the eastern North Pacific compared to the best forecasts (Figs. 13g,h and Fig. 14d). Consequently, the presence of higher geopotential height anomalies over the eastern North Pacific at the time of forecast initialization is a noticeable differentiator between the worst and best forecasts regardless of the prevailing NPJ regime.

Substantial differences in the upper-tropospheric flow pattern over the North Pacific are observed 192 h following the initialization of a best and worst forecast, respectively. In particular, the upper-tropospheric flow pattern 192 h following the initialization of a best forecast is characterized by an anomalous trough over the high-latitude North Pacific and an anomalous ridge over the subtropical North Pacific that, in combination, favor an extended and poleward-shifted NPJ regardless of the NPJ regime at the time of forecast initialization (Figs. 15a,c,e,g). Downstream of the trough over the high-latitude North Pacific, an anomalous ridge is also firmly positioned over North America in the best forecast composites. In contrast, the upper-tropospheric flow pattern 192 h following the initialization of a worst forecast features an

anomalous ridge over the high-latitude North Pacific and a retracted NPJ regardless of the NPJ regime at the time of forecast initialization (Figs. 15b,d,f,h). An anomalous trough of variable strength is also located over North America downstream of the high-latitude North Pacific ridge in all of the worst forecast composites.

The difference between the geopotential height anomalies 192 h following the initialization of a worst and best forecast is clearly identified in Fig. 16. Compared to the best forecast composites, the worst forecast composites exhibit significantly higher geopotential height anomalies over the high-latitude North Pacific, and significantly lower geopotential height anomalies over the subtropical North Pacific (Figs. 16a,b,c,d), reminiscent of a Rex block (Rex 1950). Notably, this difference pattern prevails regardless of the NPJ regime at the time of forecast initialization. Consequently, the upper-tropospheric flow patterns shown in Figs. 13 and 15 uniformly suggest that periods characterized by the development and/or maintenance of upper-tropospheric blocking events over the North Pacific are associated with reduced forecast skill with respect to the NPJ Phase Diagram. Conversely, those periods that evolve towards a zonal flow pattern over the North Pacific are generally associated with enhanced forecast skill.

6. Discussion and conclusions

The preceding analysis corroborates the results from prior studies of NPJ variability that establish a connection between the two leading modes of 250-hPa zonal wind variability over the North Pacific and the large-scale flow pattern over North America (e.g., Athanasiadis et al. 2010; Jaffe et al. 2011; Griffin and Martin 2017). Provided with this connection, this study utilizes the two leading modes of 250-hPa zonal wind variability from the CFSR during the cool season as the foundation for developing a NPJ Phase Diagram. The NPJ Phase Diagram subsequently provides an objective tool to monitor the state and evolution of the upper-tropospheric flow

pattern over the North Pacific, to identify the prevailing NPJ regime, and to evaluate the characteristic forecast skill associated with each NPJ regime.

The application of the NPJ Phase Diagram to 250-hPa zonal wind data from the CFSR during September–May 1979–2014 illuminates several salient characteristics of each NPJ regime and highlights opportunities for future research. In particular, while the mean and median residence times within a particular NPJ regime are typically on the order of three days, a NPJ regime can persist for multiple weeks. Furthermore, it is apparent that the frequency of each NPJ regime exhibits considerable interannual and intraannual variability. Given the relationship between each NPJ regime and the large-scale flow pattern over North America, further investigation into the large-scale flow patterns that are conducive to prolonged residence times within a NPJ regime, or that increase the frequency of a NPJ regime, may offer considerable value to operational seasonal and subseasonal forecasts over North America.

Large-scale atmospheric teleconnection patterns can strongly modulate the frequency of each NPJ regime. For example, it was noted that a positive (negative) PNA is most frequently characterized by jet extensions and poleward shifts (jet retractions and equatorward shifts). However, recall from Figs. 6a and 6c that jet extensions and poleward shifts are associated with distinctly different lower-tropospheric temperature anomalies over North America, with jet extensions favoring anomalously cold temperatures over eastern North America and poleward shifts favoring anomalously warm temperatures over northern North America. Consequently, knowledge of the prevailing NPJ regime provides additional operational value beyond sole knowledge of the PNA index when evaluating the character of the large-scale flow pattern over North America. The NPJ Phase Diagram provides an objective basis for detailed investigations of NPJ variability during other well-established atmospheric teleconnection patterns, as well,

such as the AO, ENSO, North Atlantic Oscillation (e.g., Wallace and Gutzler 1981), and Madden–Julian Oscillation (Madden and Julian 1972). Such investigations may offer additional value to seasonal and subseasonal forecasts by illuminating the palette of large-scale flow evolutions over the North Pacific that may operate during a particular atmospheric teleconnection pattern.

Knowledge of the relative forecast skill associated with each NPJ regime illuminates particular periods during the cool season that may be characterized by enhanced or reduced forecast skill. In particular, the frequency distribution of the worst forecasts with respect to the NPJ Phase Diagram exhibits a bimodal structure throughout the duration of an individual cool season, with relative maxima during December and March, and a relative minimum during January. While it is clear that ensemble mean forecasts initialized during the winter generally exhibit the largest distance errors within the NPJ Phase Diagram, additional research is necessary to affirm the veracity of the relative frequency minimum that characterizes the worst NPJ Phase Diagram forecasts during January and to identify factors that may contribute to its occurrence.

Examination of the forecast skill associated with each NPJ regime offers additional insight into the types of large-scale flow patterns that exhibit reduced forecast skill. Overall, the analysis persistently indicates that forecasts verified during jet retractions and equatorward shifts exhibit reduced forecast skill with respect to the NPJ Phase Diagram compared to jet extensions and poleward shifts. Recall from the NPJ composites in Figs. 5 and 6, that these particular NPJ regimes are associated with the development of anomalous ridges in the central and high-latitude North Pacific, respectively. In light of this observation, it is likely that diabatic processes account for some of the reduced forecast skill associated with these NPJ regimes, given the documented ability of diabatic processes to amplify the flow pattern, (e.g., Massacand et al. 2001; Riemer et

al. 2008; Torn 2010; Ferranti et al. 2015; Pfahl et al. 2015; Grams and Archambault 2016; Bosart et al. 2017). Additional case study work that utilizes the NPJ Phase Diagram to interrogate poor forecasts verified during jet retractions and equatorward shifts is likely to illuminate the specific processes that contribute to the reduced forecast skill during these NPJ regimes.

An examination of the best and worst medium-range forecasts with respect to the NPJ Phase Diagram suggests that the worst forecasts are associated with the development and/or maintenance of upper-tropospheric blocking events over the North Pacific. This result holds regardless of the NPJ regime at the time of forecast initialization, and corroborates previous work highlighting the reduced predictability associated with the development of upper-tropospheric blocking events (e.g., Tibaldi and Molteni 1990; D’Andrea et al. 1998; Frederiksen et al. 2004; Pelly and Hoskins 2006; Matsueda 2011; Ferranti et al. 2015). Consequently, greater understanding surrounding the variability of large-scale flow evolutions that are conducive to the development of upper-tropospheric blocking events is necessary. The NPJ Phase Diagram provides an objective frame of reference from which to examine the development of upper-tropospheric blocking events and to identify the spectrum of large-scale flow evolutions that are conducive to block formation. Additionally, it is apparent that the worst forecasts are associated with a significant movement of the NPJ towards an equatorward shift within the NPJ Phase Diagram during the 10-day period following forecast initialization, while the best forecasts are associated with a significant movement of the NPJ towards a poleward shift. In light of this result, the NPJ Phase Diagram provides an objective tool to identify NPJ regime transitions and can be utilized to examine the characteristic large-scale flow patterns associated with those transitions. Results from such examinations have the potential to increase confidence in

operational forecasts during periods of NPJ regime transition, given that certain trajectories within the NPJ Phase Diagram are associated with reduced forecast skill.

Finally, the relative forecast skill associated with each NPJ regime is only applicable with respect to the GEFS Reforecast dataset. Consequently, additional research is required to evaluate the forecast skill of NPJ regimes with respect to other ensemble prediction systems. An independent evaluation of forecast skill with respect to these other ensemble prediction systems has the potential to illuminate whether the large-scale flow patterns that exhibit reduced skill in the GEFS Reforecast dataset are pervasive across all modeling systems. To the degree that any differences exist between ensemble prediction systems with respect to the relative forecast skill of each NPJ regime, these evaluations have the potential to identify situations during which greater confidence can be prescribed to a particular ensemble prediction system.

Acknowledgments

The authors thank Mike Bodner, Daniel Halperin, Arlene Laing, Bill Lamberson, Sara Ganetis, and Josh Kastman for their constructive discussions concerning the NPJ Phase Diagram. The authors also thank the National Oceanic and Atmospheric Administration for its support of this work via Grant NA15NWS4680006.

REFERENCES

- Ambaum, M. H. P., B. J. Hoskins, and D. B. Stephenson, 2001: Arctic Oscillation or North Atlantic Oscillation? *J. Climate*, **14**, 3495–3507, doi: 10.1175/1520-0442(2001)014<3495:AOONAO>2.0.CO;2.
- Archambault, H. M., L. F. Bosart, D. Keyser, and J. M. Cordeira, 2013: A climatological analysis of the extratropical flow response to recurving western North Pacific tropical cyclones. *Mon. Wea. Rev.*, **141**, 2325–2346, doi: 10.1175/MWR-D-12-00257.1.
- Archambault, H. M., D. Keyser, L. F. Bosart, C. A. Davis, and J. M. Cordeira, 2015: A composite perspective of the extratropical flow response to recurving western North Pacific tropical cyclones. *Mon. Wea. Rev.*, **143**, 1122–1141, doi: 10.1175/MWR-D-14-00270.1.
- Athanasiadis, P. J., J. M. Wallace, and J. J. Wettstein, 2010: Patterns of wintertime jet stream variability and their relation to the storm tracks. *J. Atmos. Sci.*, **67**, 1361–1381, doi: 10.1175/2009JAS3270.1.
- Barnston, A. G., and R. E. Livezey, 1987: Classification, seasonality and persistence of low-frequency atmospheric circulation patterns. *Mon. Wea. Rev.*, **115**, 1083–1126, doi: 10.1175/1520-0493(1987)115<1083:CSAPOL>2.0.CO;2.
- Bosart, L. F., B. J. Moore, J. M. Cordeira, and H. M. Archambault, 2017: Interactions of North Pacific tropical, midlatitude, and polar disturbances resulting in linked extreme weather events over North America in October 2007. *Mon. Wea. Rev.*, **145**, 1245–1273, doi: 10.1175/MWR-D-16-0230.1.
- Chang, E. K. M., S. Lee, and K. L. Swanson, 2002: Storm track dynamics. *J. Climate*, **15**, 2163–2183, doi: 10.1175/1520-0442(2002)015<02163:STD>2.0.CO;2.

655 Cook, A. R., L. M. Leslie, D. B. Parsons, and J. T. Schaefer, 2017: The impact of El Niño–
 656 Southern Oscillation (ENSO) on winter and early spring U.S. tornado outbreaks. *J. Appl.*
 657 *Meteor. Climatol.*, **56**, 2455–2478, doi: 10.1175/JAMC-D-16-0249.1.
 658 CPC, 2017a: Pacific/North American pattern. Accessed 9 February 2017,
 659 <http://www.cpc.ncep.noaa.gov/products/precip/CWlink/pna/pna.shtml>.
 660 CPC, 2017b: Arctic Oscillation. Accessed 9 February 2017,
 661 http://www.cpc.ncep.noaa.gov/products/precip/CWlink/daily_ao_index/ao.shtml.
 662 D’Andrea, F., and Coauthors, 1998: Northern Hemisphere atmospheric blocking as simulated by
 663 15 atmospheric general circulation models in the period 1979–1988. *Climate Dyn.*, **14**,
 664 385–407, doi: 10.1007/s003820050230.
 665 Eichelberger, S. J., and D. L. Hartmann, 2007: Zonal jet structure and the leading mode of
 666 variability. *J. Climate*, **20**, 5149–5163, doi: 10.1175/JCLI4279.1.
 667 ESRL, 2017: Niño 3.4 SST Index. Accessed 5 January 2017,
 668 https://www.esrl.noaa.gov/psd/gcos_wgsp/Timeseries/Nino34/.
 669 Ferranti, L., S. Corti, and M. Janousek, 2015: Flow-dependent verification of the ECMWF
 670 ensemble over the Euro-Atlantic sector. *Quart. J. Roy. Meteor. Soc.*, **141**, 916–924, doi:
 671 10.1002/qj.2411.
 672 Franzke, C., and S. B. Feldstein, 2005: The continuum and dynamics of Northern Hemisphere
 673 teleconnection patterns. *J. Atmos. Sci.*, **62**, 3250–3267, doi: 10.1175/JAS3536.1.
 674 Franzke, C., S. B. Feldstein, and S. Lee, 2011: Synoptic analysis of the Pacific–North American
 675 teleconnection pattern. *Quart. J. Roy. Meteor. Soc.*, **137**, 329–346, doi:
 676 <https://doi.org/10.1002/qj.768>.

677 Frederiksen, J. S., M. A. Collier, and A. B. Watkins, 2004: Ensemble prediction of blocking
 678 regime transitions. *Tellus*, **56A**, 485–500, doi: 10.1111/j.1600-0870.2004.00075.x.
 679 Grams, C. M., and H. M. Archambault, 2016: The key role of diabatic outflow in amplifying the
 680 midlatitude flow: A representative case study of weather systems surrounding western
 681 North Pacific extratropical transition. *Mon. Wea. Rev.*, **144**, 3847–3869, doi:
 682 10.1175/MWR-D-15-0419.1.
 683 Griffin, K. S., and J. E. Martin, 2017: Synoptic features associated with temporally coherent
 684 modes of variability of the North Pacific jet stream. *J. Climate*, **30**, 39–54, doi:
 685 10.1175/JCLI-D-15-0833.1.
 686 Hakim, G. J., 2003: Developing wave packets in the North Pacific storm track. *Mon. Wea. Rev.*,
 687 **131**, 2824–2837, doi: 10.1175/1520-0493(2003)131<2824:DWPITN>2.0.CO;2.
 688 Harr, P. A., and J. M. Dea, 2009: Downstream development associated with the extratropical
 689 transition of tropical cyclones over the western North Pacific. *Mon. Wea. Rev.*, **137**,
 690 1295–1319, doi: 10.1175/2008MWR2558.1.
 691 Hamill, T. M., G. T. Bates, J. S. Whitaker, D. R. Murray, M. Fiorino, T. J. Galarneau Jr., Y. Zhu,
 692 and W. Lapenta, 2013: NOAA’s second-generation global medium-range ensemble
 693 reforecast dataset. *Bull. Amer. Meteor. Soc.*, **94**, 1553–1565, doi: 10.1175/BAMS-D-12-
 694 00014.1.
 695 Handlos, Z. J., and J. E. Martin, 2016: Composite analysis of large-scale environments
 696 conducive to western Pacific polar/subtropical jet superposition. *J. Climate*, **29**, 7145–
 697 7165, doi: 10.1175/JCLI-D-16-0044.1.

698 Higgins, R. W., J.-K. E. Schemm, W. Shi, and A. Leetmaa, 2000: Extreme precipitation events
 699 in the western United States related to tropical forcing. *J. Climate*, **13**, 793–820, doi:
 700 10.1175/1520-0442(2000)013<0793:EPEITW>2.0.CO;2.

701 Horel, J. D., and J. M. Wallace, 1981: Planetary-scale atmospheric phenomena associated with
 702 the Southern Oscillation. *Mon. Wea. Rev.*, **109**, 813–829, doi: 10.1175/1520-
 703 0493(1981)109<0813:PSAPAW>2.0.CO;2.

704 Hoskins, B. J., and D. J. Karoly, 1981: The steady linear response of a spherical atmosphere to
 705 thermal and orographic forcing. *J. Atmos. Sci.*, **38**, 1179–1196, doi: 10.1175/1520-
 706 0469(1981)038<1179:TSLROA>2.0.CO;2.

707 Jaffe, S. C., J. E. Martin, D. J. Vimont, and D. J. Lorenz, 2011: A synoptic climatology of
 708 episodic, subseasonal retractions of the Pacific jet. *J. Climate*, **24**, 2846–2860, doi:
 709 10.1175/2010JCLI3995.1.

710 Jhun, J.-G., and E.-J. Lee, 2004: A new East Asian winter monsoon index and associated
 711 characteristics of the winter monsoon. *J. Climate*, **17**, 711–726, doi: 10.1175/1520-
 712 0442(2004)017<0711:ANEAWM>2.0.CO;2.

713 Kalnay, E., and Coauthors, 1996: The NCEP/NCAR 40-year reanalysis project. *Bull. Amer.*
 714 *Meteor. Soc.*, **77**, 437–471, doi: 10.1175/1520-0477(1996)077<0437:TNYRP>2.0.CO;2.

715 Lee, Y.-Y., G.-H. Lim, and J.-S. Kug, 2010: Influence of the East Asian winter monsoon on the
 716 storm track activity over the North Pacific. *J. Geophys. Res.*, **115**, D09102, doi:
 717 10.1029/2009JD012813.

718 Lillo, S. P., and D. B. Parsons, 2017: Investigating the dynamics of error growth in ECMWF
 719 medium-range forecast busts. *Quart. J. Roy. Meteor. Soc.*, **143**, 1211–1226, doi:
 720 10.1002/qj.2938.

721 Lin, H., and J. Derome, 1996: Changes in predictability associated with the PNA pattern. *Tellus*,
722 **48A**, 553–571, doi: 10.1034/j.1600-0870.1996.t01-3-00005.x.

723 Madden, R. A., and P. R. Julian, 1972: Description of global-scale circulation cells in the tropics
724 with a 40–50 day period. *J. Atmos. Sci.*, **29**, 1109–1123, doi: 10.1175/1520-
725 0469(1972)029<1109:DOGSCC>2.0.CO;2.

726 Madden, R. A., and P. R. Julian, 1994: Observations of the 40–50-day tropical oscillation—A
727 review. *Mon. Wea. Rev.*, **122**, 814–837, doi: 10.1175/1520-
728 0493(1994)122<0814:OOTDTO>2.0.CO;2.

729 Massacand, A. C., H. Wernli, and H. C. Davies, 2001: Influence of upstream diabatic heating
730 upon an alpine event of heavy precipitation. *Mon. Wea. Rev.*, **129**, 2822–2828, doi:
731 10.1175/1520-0493(2001)129<2822:IOUDHU>2.0.CO;2.

732 Matsueda, M., 2011: Predictability of Euro-Russian blocking in summer of 2010. *Geophys. Res.*
733 *Lett.*, **38**, L06801, doi: 10.1029/2010GL046557.

734 North, G. R., T. L. Bell, R. F. Cahalan, and F. J. Moeng, 1982: Sampling errors in the estimation
735 of empirical orthogonal functions. *Mon. Wea. Rev.*, **110**, 699–706, doi: 10.1175/1520-
736 0493(1982)110<0699:SEITEO>2.0.CO;2.

737 Orlanski, I., and J. P. Sheldon, 1995: Stages in the energetics of baroclinic systems. *Tellus*, **47A**,
738 605–628, doi: 10.1034/j.1600-0870.1995.00108.x.

739 Palmer, T. N., 1988: Medium and extended range predictability and stability of the Pacific/North
740 American mode. *Quart. J. Roy. Meteor. Soc.*, **114**, 691–713. doi:
741 10.1002/qj.49711448108.

742 Pelly J. L., and B. J. Hoskins, 2006: How well does the ECMWF Ensemble Prediction System
743 predict blocking? *Quart. J. Roy. Meteor. Soc.*, **129**, 1683–1702, doi: 10.1256/qj.01.173.

744 Pfahl, S., C. Schwierz, M. Croci-Maspoli, C. M. Grams, and H. Wernli, 2015: Importance of
 745 latent heat release in ascending air streams for atmospheric blocking. *Nat. Geosci.*, **8**,
 746 610–614, doi: 10.1038/ngeo2487.

747 Rasmusson, E. M., and J. M. Wallace, 1983: Meteorological aspects of the El Niño/Southern
 748 Oscillation. *Science*, **222**, 1195–1202, doi: 10.1126/science.222.4629.1195.

749 Rasmusson, E. M., and K. Mo, 1993: Linkages between 200-mb tropical and extratropical
 750 circulation anomalies during the 1986–1989 ENSO cycle. *J. Climate*, **6**, 595–616, doi:
 751 10.1175/1520-0442(1993)006<0595:LBMTAE>2.0.CO;2.

752 Rex, D. F., 1950: Blocking action in the middle troposphere and its effect upon regional climate.
 753 I: An aerological study of blocking action. *Tellus*, **2A**, 196–211, doi: 10.1111/j.2153-
 754 3490.1950.tb00331.x.

755 Riemer, M., S. C. Jones, and C. A. Davis, 2008: The impact of extratropical transition on the
 756 downstream flow: An idealized modelling study with a straight jet. *Quart. J. Roy.
 757 Meteor. Soc.*, **134**, 69–91, doi: 10.1002/qj.189.

758 Saha, S., and Coauthors, 2010: The NCEP Climate Forecast System Reanalysis. *Bull. Amer.
 759 Meteor. Soc.*, **91**, 1015–1057, doi: 10.1175/2010BAMS3001.1.

760 Saha, S., and Coauthors, 2014: The NCEP Climate Forecast System version 2. *J. Climate*, **27**,
 761 2185–2208, doi: 10.1175/JCLI-D-12-00823.1.

762 Schubert, S. D., and C.-K. Park, 1991: Low-frequency intraseasonal tropical–extratropical
 763 interactions. *J. Atmos. Sci.*, **48**, 629–650, doi: 10.1175/1520-
 764 0469(1991)048<0629:LFITEI>2.0.CO;2.

765 Sheng, J., 2002: GCM experiments on changes in atmospheric predictability associated with the
 766 PNA pattern and tropical SST anomalies. *Tellus*, **54A**, 317–329, doi: 10.1034/j.1600-
 767 0870.2002.01324.x.

768 Strong, C., and R. E. Davis, 2008: Variability in the position and strength of winter jet stream
 769 cores related to Northern Hemisphere teleconnections. *J. Climate*, **21**, 584–592, doi:
 770 10.1175/2007JCLI1723.1.

771 Tibaldi, S., and F. Molteni, 1990: On the operational predictability of blocking. *Tellus*, **42A**,
 772 343–365, doi: 10.1034/j.1600-0870.1990.t01-2-00003.x.

773 Thompson, D. W. J., and J. M. Wallace, 1998: The Arctic oscillation signature in wintertime
 774 geopotential height and temperature fields. *Geophys. Res. Lett.*, **25**, 1297–1300, doi:
 775 10.1029/98GL00950.

776 Torn, R. D., 2010: Diagnosis of the downstream ridging associated with extratropical transition
 777 using short-term ensemble forecasts. *J. Atmos. Sci.*, **67**, 817–833, doi:
 778 10.1175/2009JAS3093.1.

779 Torn, R. D., and G. J. Hakim, 2015: Comparison of wave packets associated with extratropical
 780 transition and winter cyclones. *Mon. Wea. Rev.*, **143**, 1782–1803, doi: 10.1175/MWR-D-
 781 14-00006.1.

782 Wallace, J. M., and D. S. Gutzler, 1981: Teleconnections in the geopotential height field during
 783 the Northern Hemisphere winter. *Mon. Wea. Rev.*, **109**, 784–812, doi: 10.1175/1520-
 784 0493(1981)109<0784:TITGHF>2.0.CO;2.

785 Wang, L., and W. Chen, 2014: An intensity index for the East Asian winter monsoon. *J. Climate*,
 786 **27**, 2361–2374, doi: 10.1175/JCLI-D-13-00086.1.

787 Weare, B. C., and J. S. Nasstrom, 1982: Examples of extended empirical orthogonal function
 788 analyses. *Mon. Wea. Rev.*, **110**, 481–485, doi:10.1175/1520-0493(1982)110,0481:
 789 EOEEOF.2.0.CO;2.

790 Wilks, D. S., 2011: Statistical Methods in the Atmospheric Sciences. 3rd ed. Elsevier, 676 pp.

791 Xie, Z., Y. Du, and S. Yang, 2015: Zonal extension and retraction of the subtropical westerly jet
 792 stream and evolution of precipitation over East Asia and the western Pacific. *J. Climate*,
 793 **28**, 6783–6798, doi: 10.1175/JCLI-D-14-00649.1.

794 Yang, S., K.-M. Lau, and K.-M. Kim, 2002: Variations of the East Asian jet stream and Asian–
 795 Pacific–American winter climate anomalies. *J. Climate*, **15**, 306–325, doi: 10.1175/1520-
 796 0442(2002)015<0306:VOTEAJ>2.0.CO;2.

797

Table Captions

TABLE 1. Characteristic residence times in days for each NPJ regime. The numbers in parentheses represent the number of unique time periods characterized by each NPJ regime during September–May 1979–2014.

TABLE 2. NPJ Phase Diagram characteristics derived from the CFSR for the periods characterized by the best and worst NPJ Phase Diagram medium-range forecasts with all quantities in expressed in PC units. $\Delta PC1$ and $\Delta PC2$ represent the change in PC 1 and PC 2, respectively, during the 10-day period following the initialization of a best and worst forecast. Asterisks indicate that values associated with the best and worst forecasts are statistically significantly different at the 99.9% confidence level.

821 **Tables**

General NPJ Regime Characteristics				
NPJ Regime	Mean Residence Time (d)	Median Residence Time (d)	Maximum Residence Time (d)	Minimum Residence Time (d)
Jet Extension (N=380)	3.85	2.50	27.25	0.25
Jet Retraction (N=383)	3.70	2.75	34.00	0.25
Poleward Shift (N=431)	3.58	2.75	18.00	0.25
Equatorward Shift (N=373)	3.65	2.50	18.50	0.25
Origin (N=872)	4.65	3.25	35.50	0.25

822

823 TABLE 1. Characteristic residence times in days for each NPJ regime. The numbers in
824 parentheses represent the number of unique time periods characterized by each NPJ regime
825 during September–May 1979–2014.

826

827

828

829

830

831

832

833

834

835

Comparison of Best/Worst Forecast Periods					
	Avg. Start PC1	Avg. Start PC2	Avg. Δ PC1	Avg. Δ PC2	Avg. 10-d Traj. Length
Best Forecasts (N=475)	0.09*	0.04	0.09	0.16*	3.50*
Worst Forecasts (N=763)	-0.18*	-0.08	0.01	-0.21*	4.33*

TABLE 2. NPJ Phase Diagram characteristics derived from the CFSR for the periods characterized by the best and worst NPJ Phase Diagram medium-range forecasts with all quantities in expressed in PC units. Δ PC1 and Δ PC2 represent the change in PC 1 and PC 2, respectively, during the 10-day period following the initialization of a best and worst forecast. Asterisks indicate that values associated with the best and worst forecasts are statistically significantly different at the 99.9% confidence level.

Figure Captions

FIG. 1. (a) September–May 250-hPa mean zonal wind is contoured in black every 10 m s^{-1} above 30 m s^{-1} , and the regression of EOF 1 onto 250-hPa zonal wind anomaly data is shaded following the legend in m s^{-1} . (b) As in (a) but for EOF 2.

FIG. 2. (a) 250-hPa wind speed in m s^{-1} is shaded following the legend at 1800 UTC 11 February 2004. (b) The location of weighted PC 1 and PC 2 at 1800 UTC 11 February 2004 within the NPJ Phase Diagram. (c),(d) As in (a),(b) but for 1800 UTC 13 March 2009.

FIG. 3. As in Fig. 2 but for (a),(b) 1800 UTC 9 April 1984 and (c),(d) 1200 UTC 28 January 1991.

FIG. 4. Schematic illustrating the classification scheme for CFSR analysis times and GEFS reforecasts with respect to the NPJ Phase Diagram.

FIG. 5. Composite mean 250-hPa wind speed in m s^{-1} is shaded in the fill pattern, 250-hPa geopotential height is contoured in black every 120 m, and 250-hPa geopotential height anomalies are contoured in solid red and dashed blue every 30 m for positive and negative values, respectively, 4 days following the initiation of a (a) jet extension, (b) jet retraction, (c) poleward shift, and (d) equatorward shift regime. Stippled areas represent locations where the 250-hPa geopotential height anomalies are statistically significantly different from climatology at the 99% confidence level.

FIG. 6. Composite anomalies of mean sea-level pressure are contoured in solid and dashed black every 2 hPa for positive and negative values, respectively, and 850-hPa temperature anomalies are shaded in the fill pattern every 1 K 4 days following the initiation of a (a) jet extension, (b) jet retraction, (c) poleward shift, and (d) equatorward shift regime. Stippled areas represent locations where the 850-hPa temperature anomalies are statistically significantly different from climatology at the 99% confidence level.

FIG. 7. (a) The percent frequency of each NPJ regime during every cool season between September 1979 and May 2014. The years indicated on the horizontal axis identify the end of individual cool seasons. (b) The percent frequency of analysis times during each month of the cool season that are characterized by each NPJ regime. The numbers in parentheses below each month indicate the number of analysis times during each month.

FIG. 8. (a) The percent frequency of each NPJ regime at analysis times during which the NPJ is outside of the unit circle on the NPJ Phase Diagram and characterized by each phase of the PNA discussed in the text. The numbers in parentheses below each category indicate the number of analysis times in each category. (b) As in (a) but for the AO. (c) As in (a) but for ENSO.

FIG. 9. (a) The average error of GEFS ensemble mean NPJ Phase Diagram forecasts initialized during the same season. The colored circles on each line indicate that the error associated with that season is statistically significantly different from the error associated with another season at the 99% confidence level. The numbers in parentheses in the legend indicate the number of forecasts in that category. Forecast lead time on the horizontal axis represents the hours after

905 forecast initialization. (b) As in (a) but for forecasts initialized during the same NPJ regime. (c)
906 As in (a) but for forecasts verified during the same NPJ regime. Forecast lead time on the
907 horizontal axis in (c) depicts the hours prior to forecast verification.

908

909 FIG. 10. The percent frequency that an NPJ regime is overforecast or underforecast by the GEFS
910 ensemble mean NPJ Phase Diagram forecasts relative to the verifying 0-h analyses at each
911 forecast lead time.

912

913 FIG. 11. Schematic illustrating the classification scheme for the best and worst NPJ Phase
914 Diagram medium-range forecasts.

915

916 FIG. 12. (a) The percent frequency of the best and worst NPJ Phase Diagram medium-range
917 forecasts that are initialized during each month of the cool season. (b) The percent frequency of
918 the best and worst NPJ Phase Diagram medium-range forecasts that are initialized during each
919 NPJ regime.

920

921 FIG. 13. Composite mean 250-hPa wind speed in m s^{-1} is shaded in the fill pattern, 250-hPa
922 geopotential height is contoured in black every 120 m, and 250-hPa geopotential height
923 anomalies are contoured in solid red and dashed blue every 30 m for positive and negative
924 values, respectively, at the time a (a) best and (b) worst NPJ Phase Diagram forecast is initialized
925 during a jet extension. (c),(d) As in (a),(b) but for those forecasts initialized during a jet
926 retraction. (e),(f) As in (a),(b) but for those forecasts initialized during a poleward shift. (g),(h)

As in (a,b) but for those forecasts initialized during an equatorward shift. The quantities in the top right corner of every panel indicate the number of cases included in each composite.

FIG. 14. (a) The difference between the 250-hPa geopotential height anomalies associated with a worst and best NPJ Phase Diagram forecast at the time of forecast initialization during a jet extension is shaded every 30 m in the fill pattern. (b) As in (a) but for a jet retraction. (c) As in (a) but for a poleward shift. (d) As in (a) but for an equatorward shift. Statistically significant differences in geopotential height anomalies at the 99% confidence level are stippled in all panels.

FIG. 15. As in Fig. 13, but for the composite 250-hPa flow pattern 192 h following the initialization of a best and worst NPJ Phase Diagram forecast.

FIG. 16. As in Fig. 14, but for the composite difference between 250-hPa geopotential height anomalies associated with the upper-tropospheric flow pattern 192 h following the initialization of a worst and best NPJ Phase Diagram forecast.

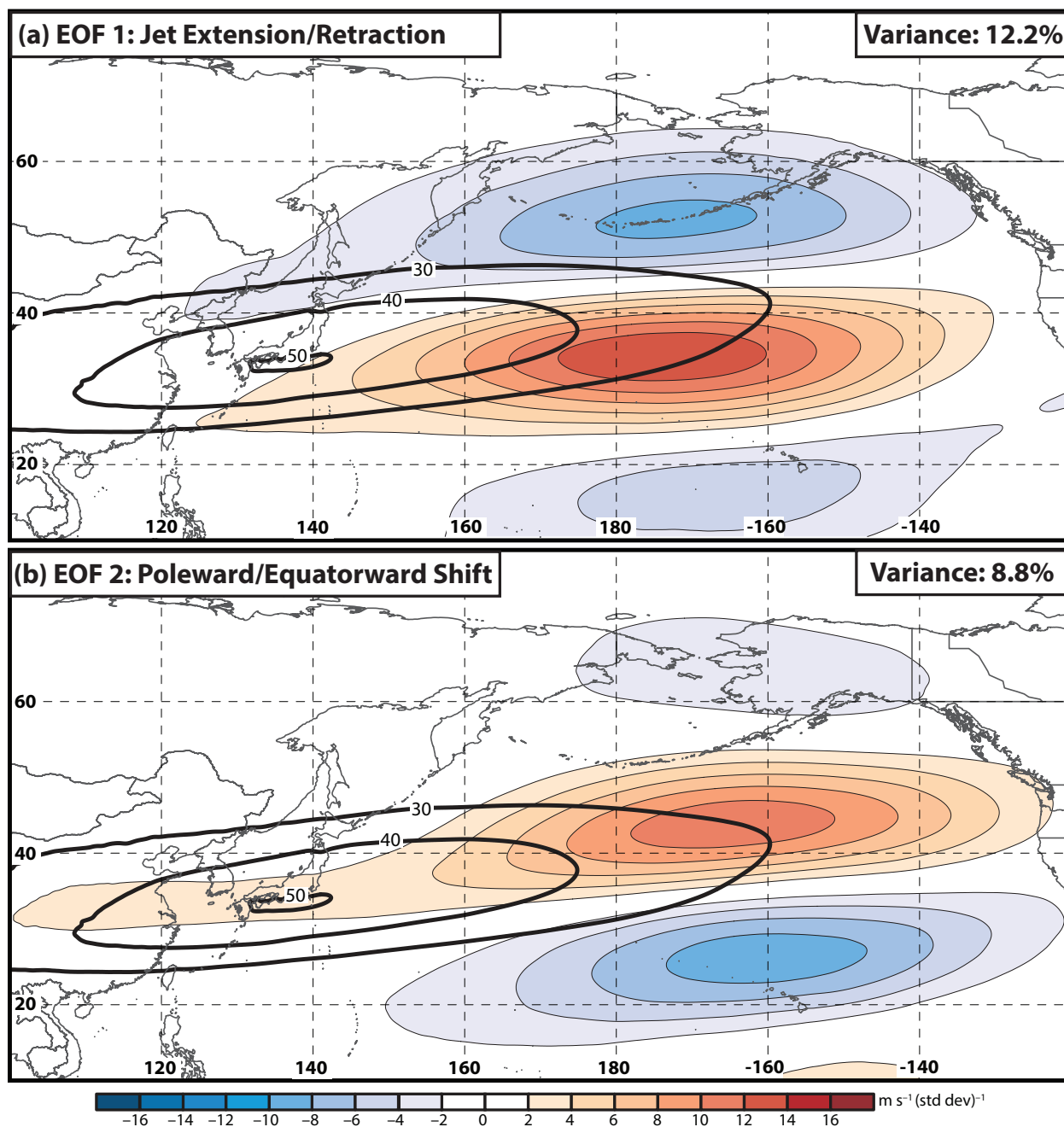


FIG. 1. (a) September–May 250-hPa mean zonal wind is contoured in black every 10 m s^{-1} above 30 m s^{-1} , and the regression of EOF 1 onto 250-hPa zonal wind anomaly data is shaded following the legend in m s^{-1} . (b) As in (a) but for EOF 2.

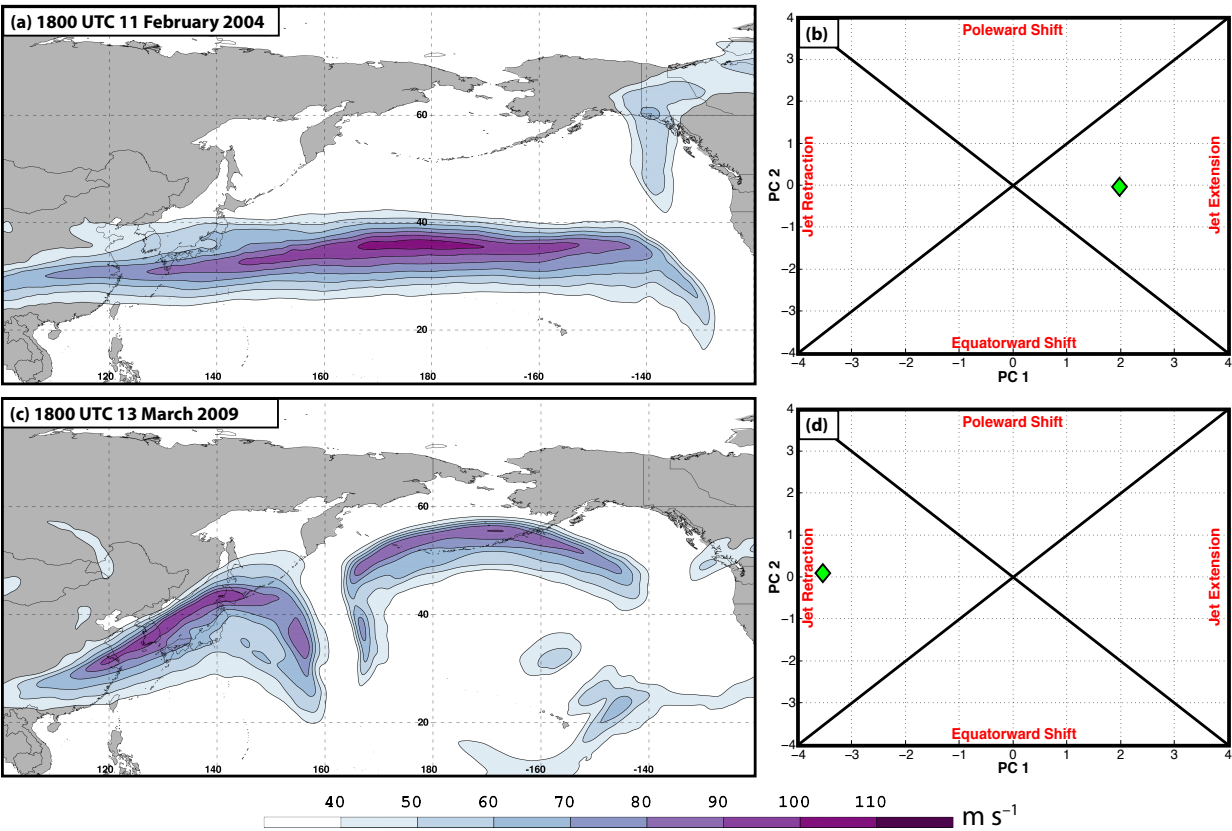


FIG. 2. (a) 250-hPa wind speed in m s^{-1} is shaded following the legend at 1800 UTC 11 February 2004. (b) The location of weighted PC 1 and PC 2 at 1800 UTC 11 February 2004 within the NPJ Phase Diagram. (c),(d) As in (a),(b) but for 1800 UTC 13 March 2009.

990

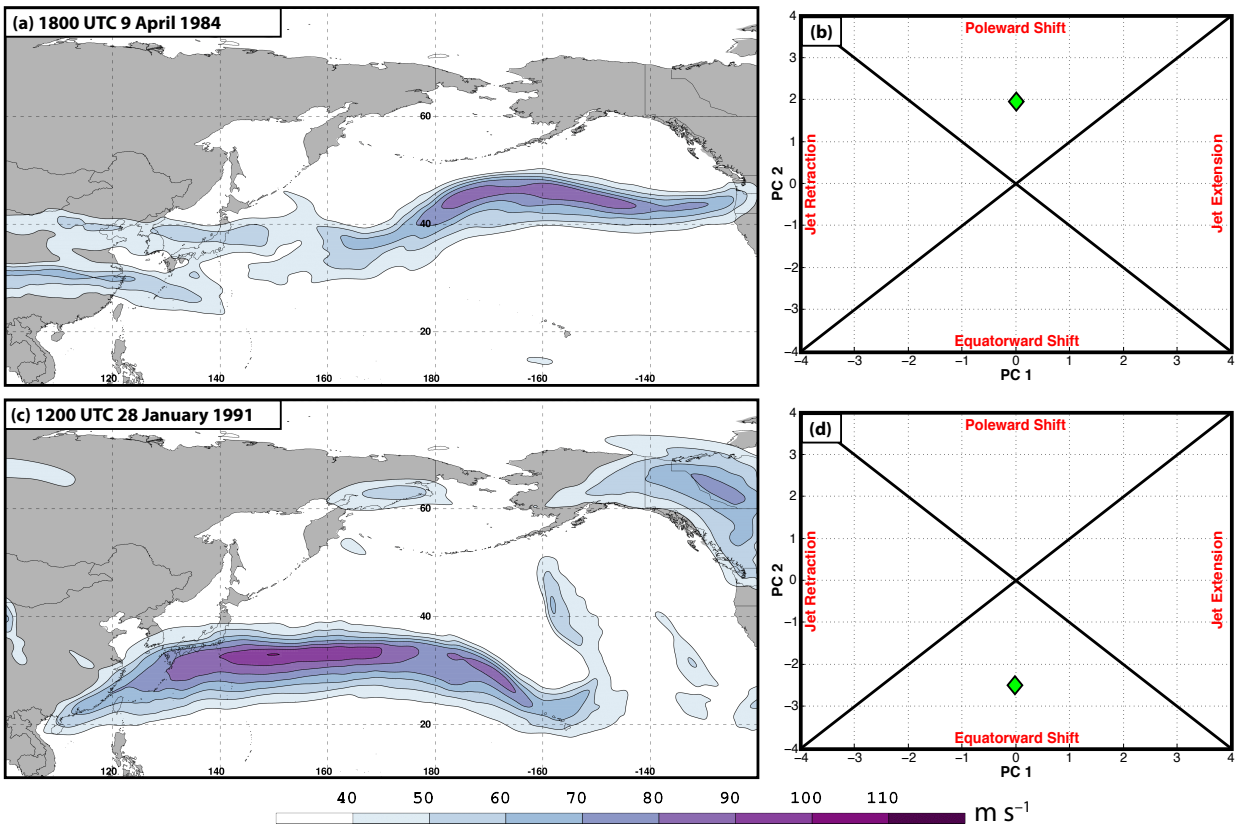
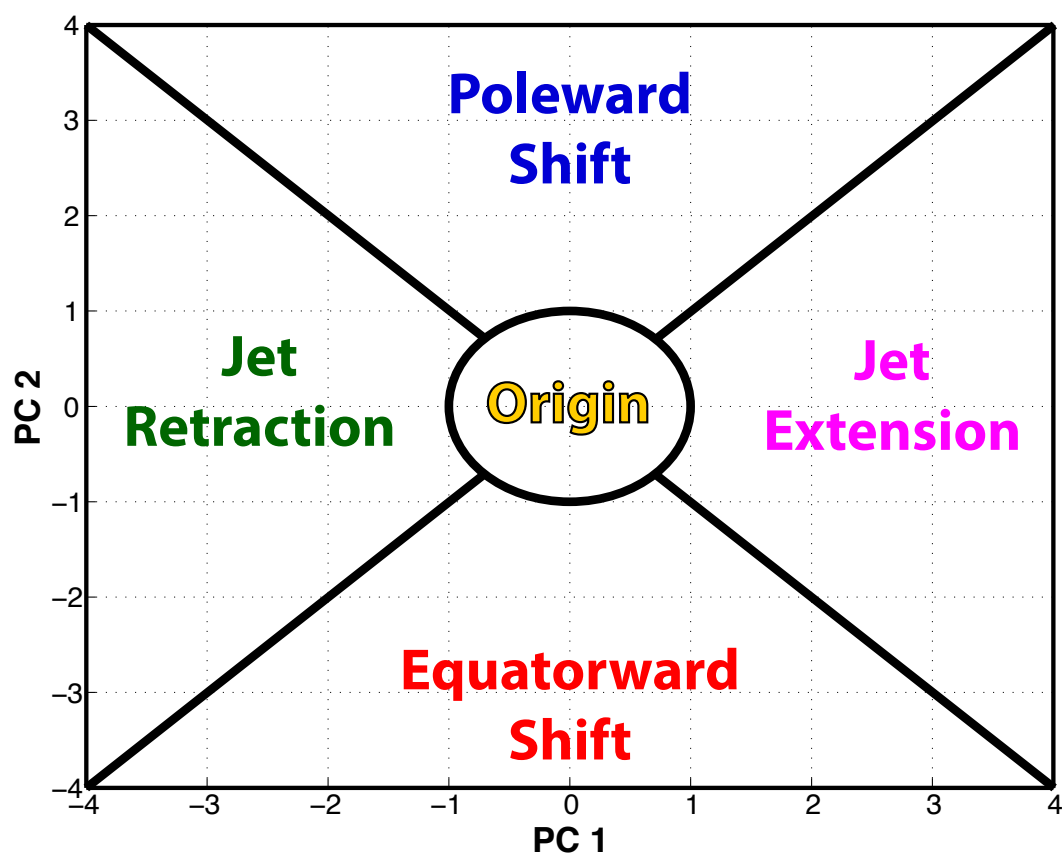


FIG. 3. As in Fig. 2 but for (a),(b) 1800 UTC 9 April 1984 and (c),(d) 1200 UTC 28 January 1991.

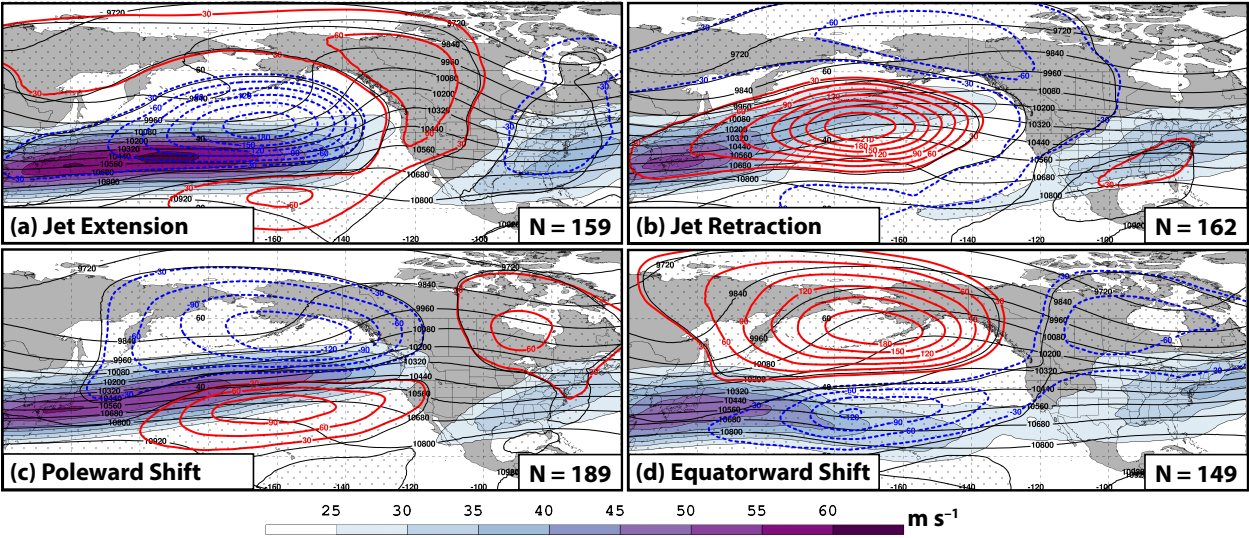
1012



1013
1014
1015
1016
1017
1018
1019
1020
1021
1022
1023
1024
1025
1026
1027
1028
1029
1030
1031
1032

FIG. 4. Schematic illustrating the classification scheme for CFSR analysis times and GEFS reforecasts with respect to the NPJ Phase Diagram.

1033



1034

1035

1036

1037

1038

1039

1040

1041

1042

1043

1044

1045

1046

1047

1048

1049

1050

1051

1052

1053

1054

1055

1056

1057

1058

1059

1060

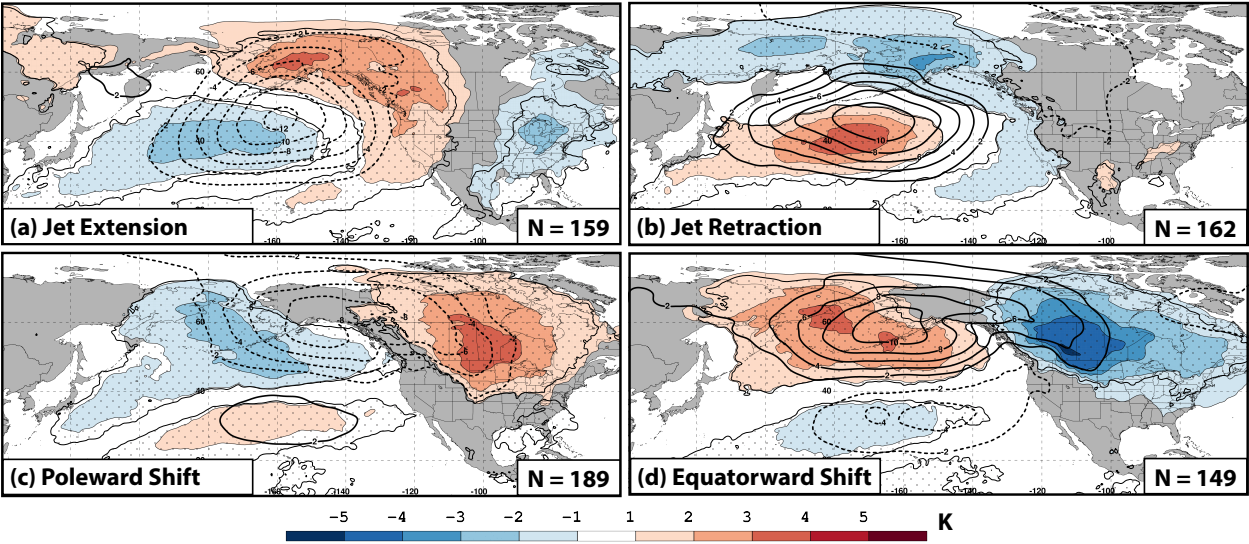
1061

1062

1063

FIG. 5. Composite mean 250-hPa wind speed in m s^{-1} is shaded in the fill pattern, 250-hPa geopotential height is contoured in black every 120 m, and 250-hPa geopotential height anomalies are contoured in solid red and dashed blue every 30 m for positive and negative values, respectively, 4 days following the initiation of a (a) jet extension, (b) jet retraction, (c) poleward shift, and (d) equatorward shift regime. Stippled areas represent locations where the 250-hPa geopotential height anomalies are statistically significantly different from climatology at the 99% confidence level.

1064



1065

1066

1067

1068

1069

1070

1071

1072

1073

1074

1075

1076

1077

1078

1079

1080

1081

1082

1083

1084

1085

1086

1087

1088

1089

1090

1091

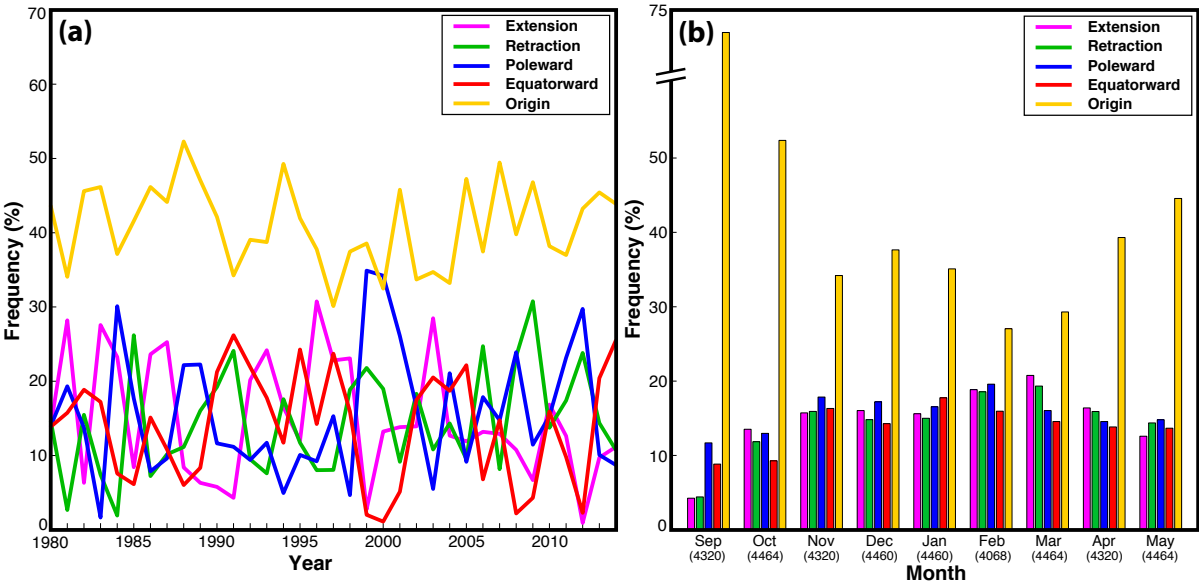
1092

1093

1094

FIG. 6. Composite anomalies of mean sea-level pressure are contoured in solid and dashed black every 2 hPa for positive and negative values, respectively, and 850-hPa temperature anomalies are shaded in the fill pattern every 1 K 4 days following the initiation of a (a) jet extension, (b) jet retraction, (c) poleward shift, and (d) equatorward shift regime. Stippled areas represent locations where the 850-hPa temperature anomalies are statistically significantly different from climatology at the 99% confidence level.

1095



1096

1097

1098

1099

1100

1101

1102

1103

1104

1105

1106

1107

1108

1109

1110

1111

1112

1113

1114

1115

1116

1117

1118

1119

1120

1121

1122

1123

1124

FIG. 7. (a) The percent frequency of each NPJ regime during every cool season between September 1979 and May 2014. The years indicated on the horizontal axis identify the end of individual cool seasons. (b) The percent frequency of analysis times during each month of the cool season that are characterized by each NPJ regime. The numbers in parentheses below each month indicate the number of analysis times during each month.

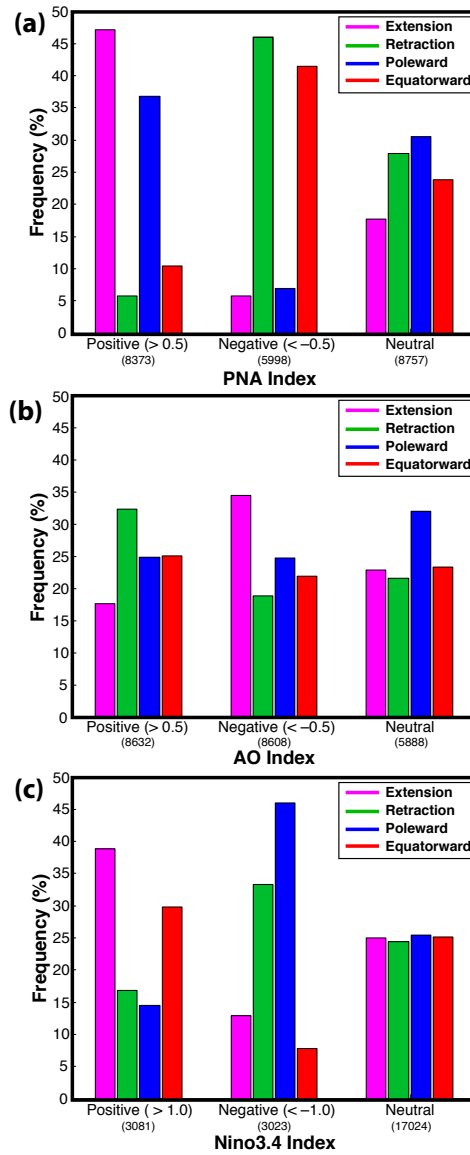


FIG. 8. (a) The percent frequency of each NPJ regime at analysis times during which the NPJ is outside of the unit circle on the NPJ Phase Diagram and characterized by each phase of the PNA discussed in the text. The numbers in parentheses below each category indicate the number of analysis times in each category. (b) As in (a) but for the AO. (c) As in (a) but for ENSO.

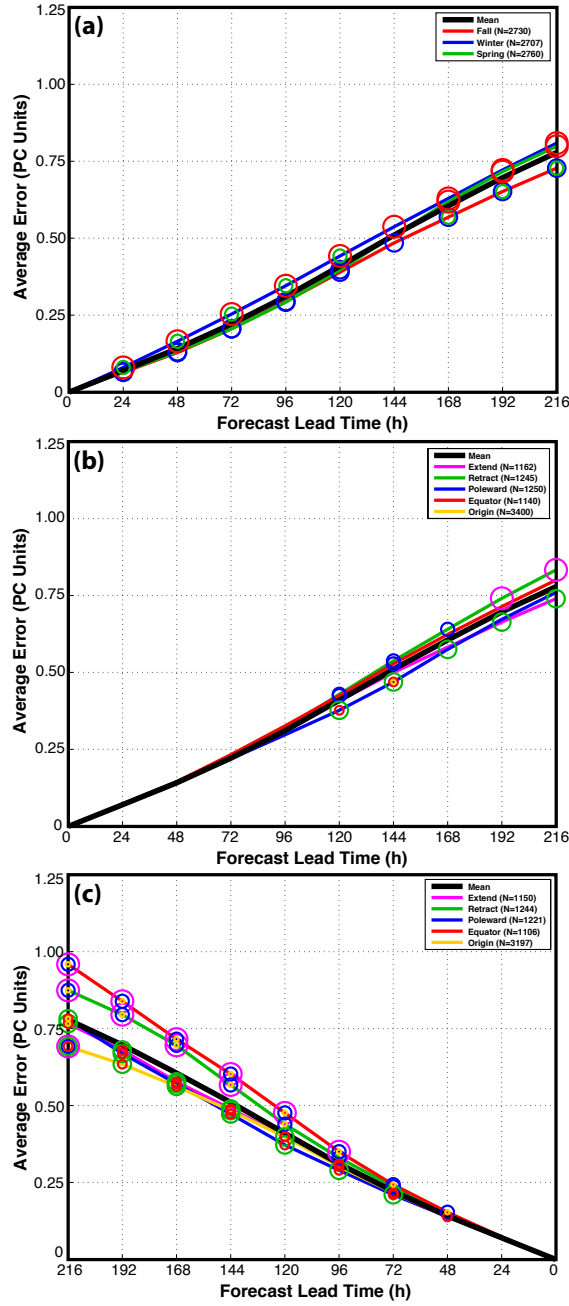
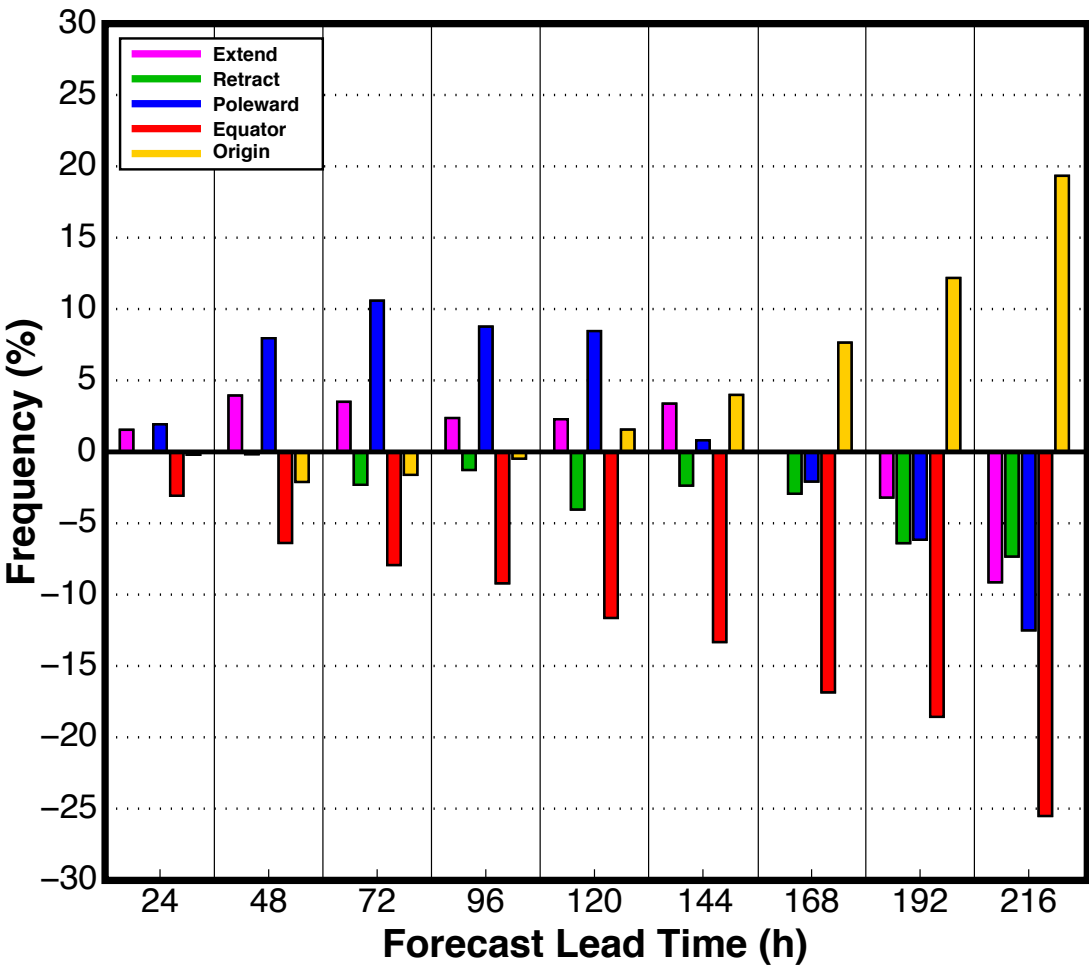


FIG. 9. (a) The average error of GEFS ensemble mean NPJ Phase Diagram forecasts initialized during the same season. The colored circles on each line indicate that the error associated with that season is statistically significantly different from the error associated with another season at the 99% confidence level. The numbers in parentheses in the legend indicate the number of forecasts in that category. Forecast lead time on the horizontal axis represents the hours after forecast initialization. (b) As in (a) but for forecasts initialized during the same NPJ regime. (c) As in (a) but for forecasts verified during the same NPJ regime. Forecast lead time on the horizontal axis in (c) depicts the hours prior to forecast verification.

1217



1218
1219
1220
1221
1222
1223
1224
1225
1226
1227
1228
1229
1230
1231
1232
1233
1234

FIG. 10. The percent frequency that an NPJ regime is overforecast or underforecast by the GEFS ensemble mean NPJ Phase Diagram forecasts relative to the verifying 0-h analyses at each forecast lead time.

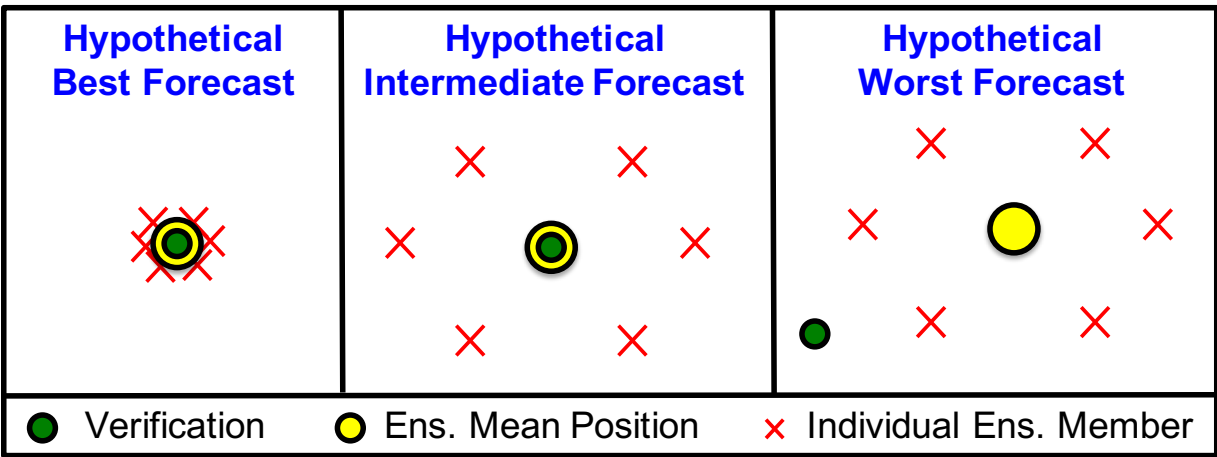


FIG. 11. Schematic illustrating the classification scheme for the best and worst NPJ Phase Diagram medium-range forecasts.

1267

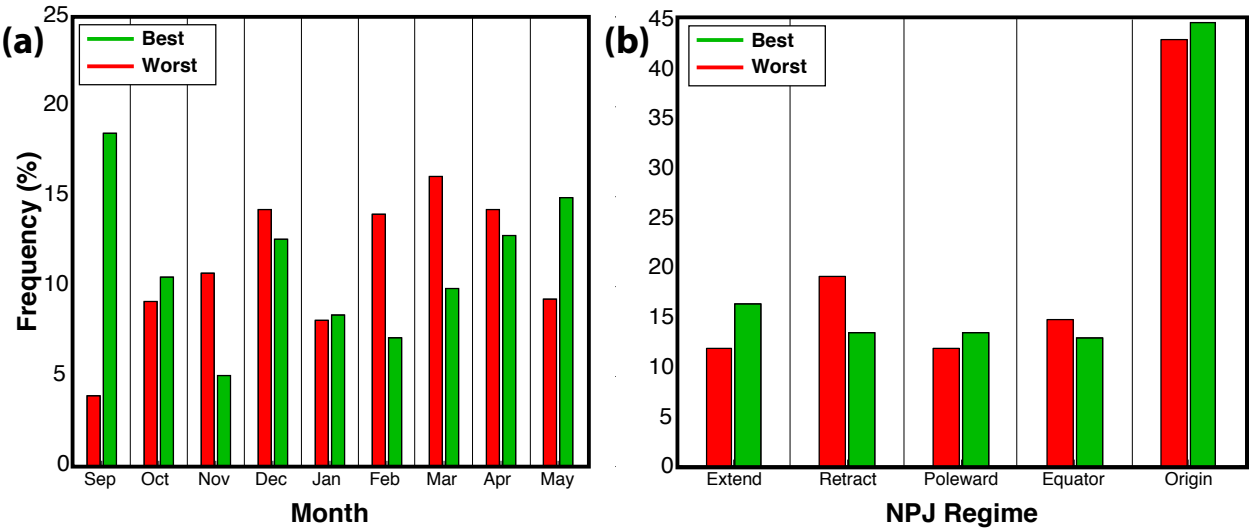


FIG. 12. (a) The percent frequency of the best and worst NPJ Phase Diagram medium-range forecasts that are initialized during each month of the cool season. (b) The percent frequency of the best and worst NPJ Phase Diagram medium-range forecasts that are initialized during each NPJ regime.

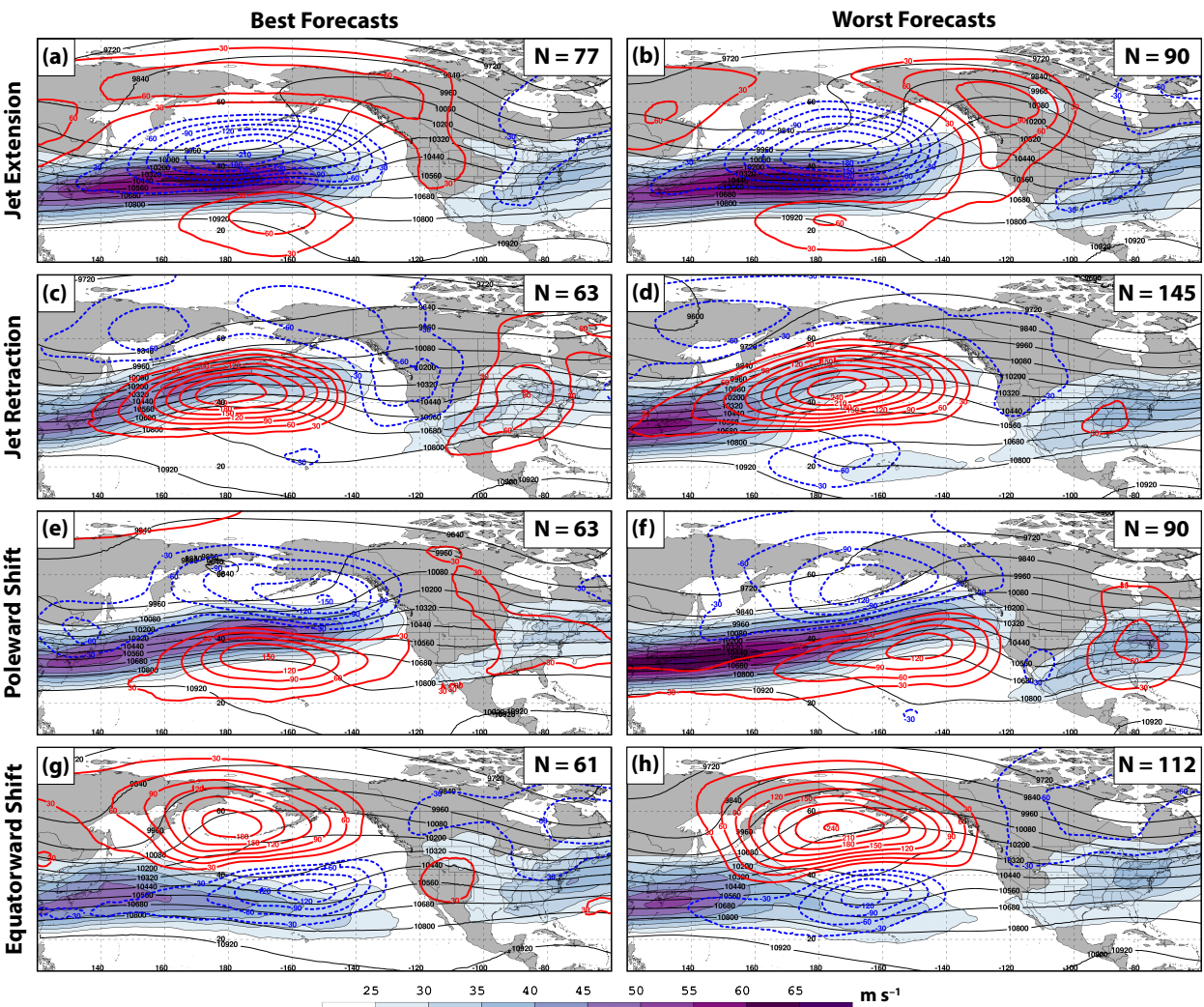


FIG. 13. Composite mean 250-hPa wind speed in m s^{-1} is shaded in the fill pattern, 250-hPa geopotential height is contoured in black every 120 m, and 250-hPa geopotential height anomalies are contoured in solid red and dashed blue every 30 m for positive and negative values, respectively, at the time a (a) best and (b) worst NPJ Phase Diagram forecast is initialized during a jet extension. (c),(d) As in (a),(b) but for those forecasts initialized during a jet retraction. (e),(f) As in (a),(b) but for those forecasts initialized during a poleward shift. (g),(h) As in (a),(b) but for those forecasts initialized during an equatorward shift. The quantities in the top right corner of every panel indicate the number of cases included in each composite.

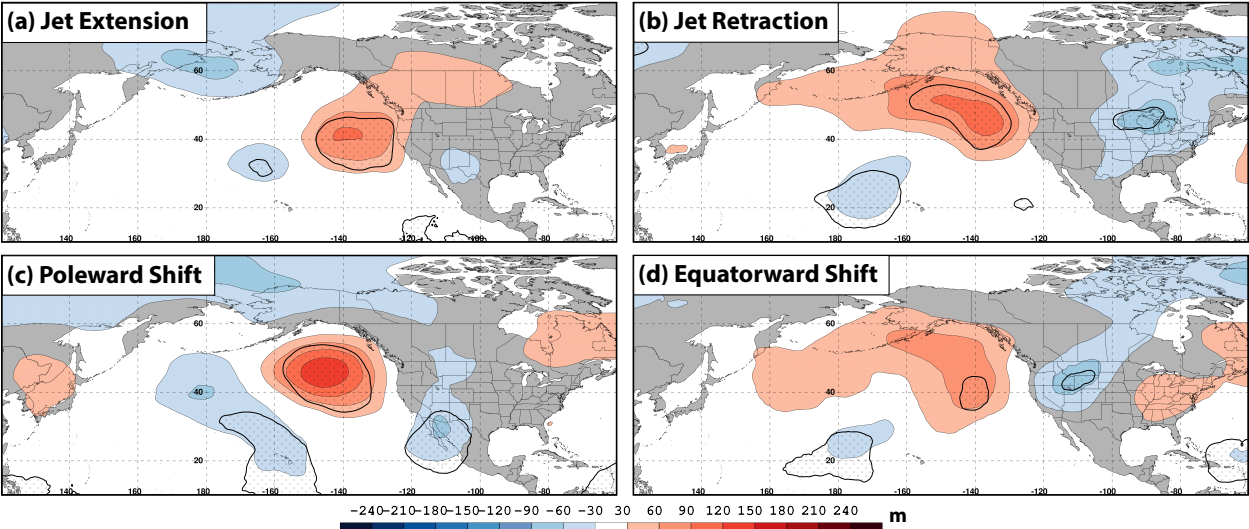
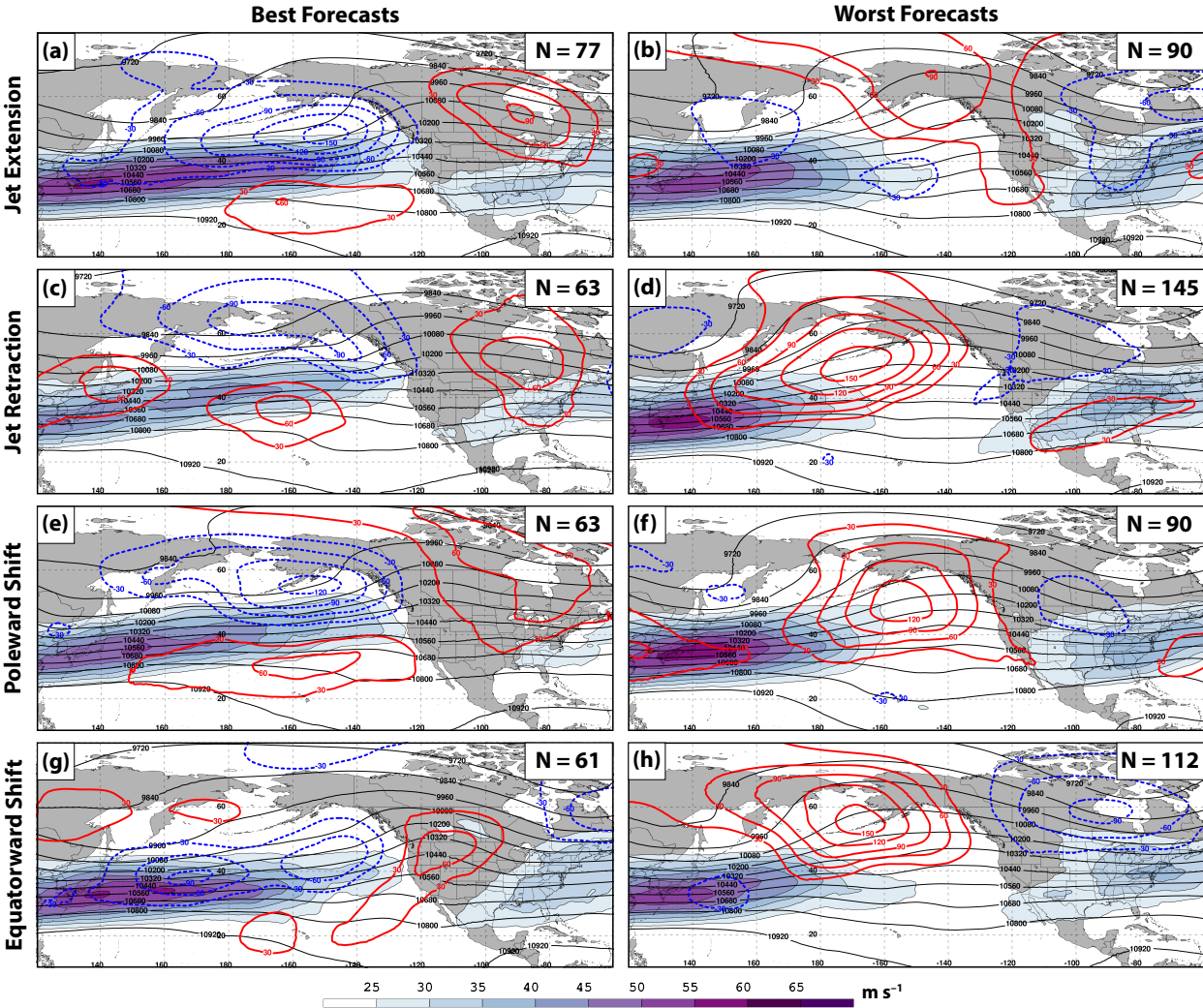


FIG. 14. (a) The difference between the 250-hPa geopotential height anomalies associated with a worst and best NPJ Phase Diagram forecast at the time of forecast initialization during a jet extension is shaded every 30 m in the fill pattern. (b) As in (a) but for a jet retraction. (c) As in (a) but for a poleward shift. (d) As in (a) but for an equatorward shift. Statistically significant differences in geopotential height anomalies at the 99% confidence level are stippled in all panels.

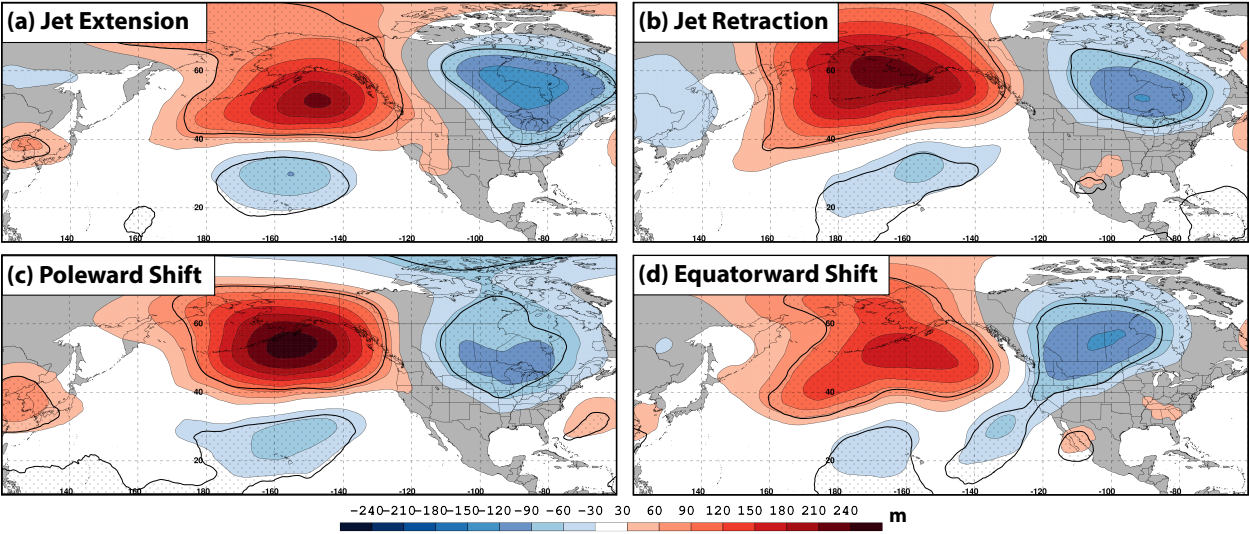
1347



1348
1349
1350
1351
1352
1353
1354
1355
1356
1357
1358
1359
1360
1361
1362
1363
1364

FIG. 15. As in Fig. 13, but for the composite 250-hPa flow pattern 192 h following the initialization of a best and worst NPJ Phase Diagram forecast.

1365



1366
1367
1368
1369
1370
1371
1372

FIG. 16. As in Fig. 14, but for the composite difference between 250-hPa geopotential height anomalies associated with the upper-tropospheric flow pattern 192 h following the initialization of a worst and best NPJ Phase Diagram forecast.